

YNOGK: A new public code for calculating null geodesics in the Kerr spacetime

Xiaolin Yang^{1,2,3}, Jiancheng Wang^{1,2}

yangxl@ynao.ac.cn

ABSTRACT

Following Dexter & Agol (2009) we present a new public code for the fast calculation of null geodesics in the Kerr spacetime. Using Weierstrass' and Jacobi's elliptic functions, we express all coordinates and affine parameters as analytical and numerical functions of a parameter p , which is an integral value along the geodesic. This is a main difference of our code compares with previous similar ones. The advantage of this treatment is that the information about the turning points do not need to be specified in advance by the user, and many applications such as imaging, the calculation of line profiles or the observer-emitter problem, etc become root finding problems. All elliptic integrations are computed by Carlson's elliptic integral method as Dexter & Agol (2009) did, which guarantees the fast computational speed of our code. The formulae to compute the constants of motion given by Cunningham & Bardeen (1973) have been extended, which allow one readily to handle the situations, in which the emitter or the observer has arbitrary distance and motion state with respect to the central compact object. The validation of the code has been extensively tested by its application to toy problems from the literature. The source FORTRAN code is freely available for download on the web.¹

Subject headings: accretion, accretion disks — black hole physics — radiative transfer — relativistic processes

¹National Astronomical Observatories, Yunnan Observatory, Chinese Academy of Sciences, Kunming 650011, China

²Key Laboratory for the Structure and Evolution of Celestial Objects, Chinese Academy of Sciences, Kunming 650011, China

³Graduate School, Chinese Academy of Sciences, Beijing, P.R. China

¹<http://www1.ynao.ac.cn/~yangxl/yxl.html>

1. Introduction

There are wide interests in calculating the radiative transfer near the compact objects, such as black hole, neutron star and white dwarf. The radiation will be affected by various effects, such as, light bending or focusing, time dilation, Doppler boosting and gravitational redshift, under the strong gravitational field of the compact objects. The consideration of these effects not only help us to understand the observed results, therefor to study these compact objects, but also even to test the correctness of the general relativity under strong gravity. A good example is the study of the fluorescent iron line in the X-ray band at 6.4-6.9 keV, which is seen in many active galactic nuclei especially for Seyfert galaxies (Laor 1991; Fabian et al. 2000; Müller & Camenzind 2004; Miniutti & Fabian 2004; Miniutti et al. 2004). The line appears broadened and skewed as a result of the Doppler effect and gravitational redshift, thus it is an important diagnostic to study the geometry and other properties of the accretion flow at the vicinity of the central black hole (Fabian et al. 2000). Another example is the study of SMBH in the center of our galaxy. It has been comprehensively accepted that in the center of our galaxy a super-massive black hole with $\sim 4 \times 10^6 M_{\odot}$ exists (Schödel et al. 2003; Gebhardt et al. 2000; Hopkins et al. 2008) and its shadow may be observed directly in the radio band in the near future. Based on the general relativistic numerical simulations of the accretion flow, Noble et al. (2007) present the first dynamically self-consistent models of millimeter and sub-millimeter emission from Sgr A^* . Yuan et al. (2009) calculated the observed images of Sgr A^* with a fully general relativistic radiative inefficient accretion flow.

A natural way to include all of the gravitational effects is to track the ray following its null geodesic orbit. Which requires the fast and accurate computations of the trajectory of a photon in the Kerr spacetime. Fanton et al. (1997) proposed a fast code to calculate the accreting lines and thin disk images. Čadež et al. (1998) translated all integrations into the Legendre’s standard elliptic integrals and wrote a fast numerical code. Dexter & Agol (2009) presented a new fast public code, named *geokerr*, for the computing of all coordinates of null geodesics in the Kerr spacetime by using the Carlson’s elliptic integrals semi-analytically for the first time. There are two computational methods often used in these codes, they are: (1) the elliptic function method, which relies on the integrability of the geodesics (Cunningham & Bardeen 1973; Cunningham 1975; Rauch & Blandford 1994; Speith et al. 1995; Fanton et al. 1997; Čadež et al. 1998; Li et al. 2005; Wu & Wang 2007; Dexter & Agol 2009; Yuan et al. 2009), and (2) the direct geodesic integration method (Fuerst & Wu 2004; Schnittman & Rezzolla 2006; Dolence et al. 2009; Anderson et al. 2010; Vincent et al. 2011; Younsi et al. 2012). Usually people regard the direct geodesic integration method to be a better choice than the elliptic function method, for the direct geodesic integration method can deal with any three-dimensional accretion flow (Younsi et al. 2012), especially in radiative transfer problems which require the calculations of many points along each geodesic, the

direct integration method is simpler and faster (Dolence et al. 2009). While the the elliptic function method is considered to be just efficient for the calculation of the emissions come from an optically thick, geometrical thin and axisymmetric accretion disk system. But we think that the elliptic function method based on Dexter & Agol (2009) after some extensions can overcome these shortages and not only handle any three-dimensional accretion flows readily, but also be more efficient, flexible, and accurate, because it can compute arbitrary points on arbitrary sections for any geodesics. The speed of the code based on this approach is still very fast for many potential applications. While the direct geodesic integration method must integrate the geodesic from the initial position to the interested points, the waste of computational time is inevitable.

We present a new public code for the computation of null geodesics in the Kerr spacetime following the work of Dexter & Agol (2009). In our code all coordinates and the affine parameters are expressed as functions of a parameter p , which corresponds to I_u or I_μ in Dexter & Agol (2009). Using parameter p as the independent variable, the computations are easier and simpler, thus more convenient, mainly due to the fact that the information about the turning points does not need to be prescribed in advance comparing with Dexter & Agol (2009). Meanwhile Yuan et al. (2009) have demonstrated that the parameter p can replace the affine parameter to be the independent variable in radiative transfer problems. We not only take this replacing, but also used it to handle more sophisticated applications. We extend the formulae of computing constants of motion from initial conditions to a more general form, which can readily handle the cases in which the emitter or the observer has arbitrary motion state and distance with respect to the central black hole. We reduce the elliptic integrals from the motion equations derived from the Hamilton-Jacobi equation (Carter 1968) to the Weierstrass' elliptic integrals rather than to the Legendre's ones, because the former ones are much easier to handle. Then we calculate these integrals by Carlson's method.

The paper is organized as follows. In section 2 we give the motion equations for null geodesics. In section 3 we express all coordinates and affine parameters as functions of a parameter p analytically and numerically. In section 4 we give the extended formulae for the computation of constants of motion. A brief introduction and discussion about the code are given in section 5. In section 6 we demonstrate the testing results of our code for toy problems in the literature. The conclusions and discussions are finally presented in section 7. The general relativity calculations follow the notational conventions of the text given by Misner et al. (1973). The natural unit are used through out this paper, in which constants $G=c=1$, and the mass of the central black hole M is also taken to be 1.

2. motion equations

Following Bardeen et al. (1972), we write the Kerr line element in the Boyer-Lindquist (B-L) coordinates (t, r, θ, ϕ) as

$$ds^2 = -e^{2\nu} dt^2 + e^{2\psi} (d\phi - \omega dt)^2 + e^{2\mu_1} dr^2 + e^{2\mu_2} d\theta^2, \quad (1)$$

where

$$\begin{aligned} e^{2\nu} &= \frac{\Sigma\Delta}{A}, & e^{2\psi} &= \frac{\sin^2\theta A}{\Sigma}, & e^{2\mu_1} &= \frac{\Sigma}{\Delta}, & e^{2\mu_2} &= \Sigma, & \omega &= \frac{2ar}{A}, \\ \Delta &= r^2 - 2r + a^2, & \Sigma &= r^2 + a^2 \cos^2\theta, & A &= (r^2 + a^2)^2 - \Delta a^2 \sin^2\theta, \end{aligned} \quad (2)$$

and a is the spin parameter of the black hole.

The geodesic equations for a freely test particle read

$$\frac{d^2 x^\alpha}{d\sigma^2} + \Gamma_{\mu\nu}^\alpha u^\mu u^\nu = 0, \quad (3)$$

where σ is the proper time for particles and an affine parameter for photons, u^ν is the four-velocity, $\Gamma_{\mu\nu}^\alpha$ is the connection coefficients. Carter (1968) found these equations are integrable under Kerr spacetime and got the differential and integral forms of motion equations for particles by using the Hamilton-Jacobi equation. For a photon, whose rest mass m is zero, the equations of motion have the following forms:

$$\Sigma \frac{dr}{d\sigma} = \pm \sqrt{R}, \quad (4)$$

$$\Sigma \frac{d\theta}{d\sigma} = \pm \sqrt{\Theta_\theta}, \quad (5)$$

$$\Sigma \frac{d\phi}{d\sigma} = -\left(a - \frac{\lambda}{\sin^2\theta}\right) + a \frac{T}{\Delta}, \quad (6)$$

$$\Sigma \frac{dt}{d\sigma} = -a(a \sin^2\theta - \lambda) + (r^2 + a^2) \frac{T}{\Delta}, \quad (7)$$

$$\pm \int^r \frac{dr}{\sqrt{R}} = \pm \int^\theta \frac{d\theta}{\sqrt{\Theta_\theta}}, \quad (8)$$

$$\sigma = \int^r \frac{r^2}{\sqrt{R}} dr + a^2 \int^\theta \frac{\cos^2\theta}{\sqrt{\Theta_\theta}} d\theta, \quad (9)$$

$$t = \sigma + 2 \int^r \frac{rT}{\Delta\sqrt{R}} dr, \quad (10)$$

$$\phi = a \int^r \frac{T}{\Delta\sqrt{R}} dr + \int^\theta \frac{\lambda \csc^2\theta - a}{\sqrt{\Theta_\theta}} d\theta, \quad (11)$$

where

$$R = r^4 - (q + \lambda^2 - a^2)r^2 + 2[q + (\lambda - a)^2]r - a^2q, \quad (12)$$

$$\Theta_\theta = q + a^2 \cos^2 \theta - \lambda^2 \cot^2 \theta, \quad (13)$$

$$T = r^2 + a^2 - \lambda a, \quad (14)$$

q and λ are constants of motion defined by

$$q = \frac{Q}{E^2}, \quad \lambda = \frac{L_z}{E}, \quad (15)$$

where Q is the Carter constant, L_z is the angular momentum of the photon about the spin axis of the black hole, E is the energy measured by an observer at infinity. The four momentum of a photon can be expressed as

$$p_\mu = E(-1, \pm \frac{\sqrt{R}}{\Delta}, \pm \sqrt{\Theta_\theta}, \lambda), \quad (16)$$

which is often used in the discussion of the motion of a photon.

From the equation (13) we know that if $q = 0$ and $\theta \equiv \pi/2$, then $\Theta_\theta \equiv 0$. $\theta \equiv \pi/2$ means the motion of the photon is confined in the equatorial plane forever (Chandrasekhar 1983). Thus the motion equations with integral forms now become invalid for $\Theta_\theta = 0$ appeared in the denominator. We need the motion equations with differential forms.

From equation (4) we have

$$\sigma_{\text{pm}} = \int^r \frac{r^2}{\sqrt{R}} dr, \quad (17)$$

where the subscript pm means 'plane motion'. Dividing equation (6) by (4) and integrating both sides, we obtain

$$\phi_{\text{pm}} = \int^r \frac{\lambda - a}{\sqrt{R}} dr + a \int^r \frac{T}{\Delta} \frac{dr}{\sqrt{R}}. \quad (18)$$

Similarly from equation (7) and (4), we obtain

$$\begin{aligned} t_{\text{pm}} &= \int^r \frac{r^2}{\sqrt{R}} dr + 2 \int^r \frac{rT}{\Delta} \frac{dr}{\sqrt{R}}, \\ &= \sigma_{\text{pm}} + 2 \int^r \frac{rT}{\Delta} \frac{dr}{\sqrt{R}}. \end{aligned} \quad (19)$$

The spherical motion is an another special case, in which the photon is confined on a sphere and the motion of which can be described by equations: $R \equiv 0$ and $dR/dr \equiv 0$ (Bardeen et al. 1972; Shakura 1987). Thus the motion equations with integral forms also

become invalid due to $R = 0$ appears in the denominator. Similarly from equation (5) we have

$$\sigma_{\text{sm}} = r^2 \int^{\theta} \frac{d\theta}{\sqrt{\Theta_{\theta}}} + \int^{\theta} \frac{a^2 \cos^2 \theta}{\sqrt{\Theta_{\theta}}} d\theta, \quad (20)$$

where the subscript sm means "spherical motion". Dividing equation (6) by (5) and integrating both sides, we have

$$\phi_{\text{sm}} = a \frac{T}{\Delta} \int^{\theta} \frac{d\theta}{\sqrt{\Theta_{\theta}}} + \int^{\theta} \frac{\lambda \csc^2 \theta - a}{\sqrt{\Theta_{\theta}}} d\theta. \quad (21)$$

From the equations (5) and (7) we have

$$t_{\text{sm}} = \sigma_{\text{sm}} + 2r \frac{T}{\Delta} \int^{\theta} \frac{d\theta}{\sqrt{\Theta_{\theta}}}. \quad (22)$$

From equation (8), we introduce a new parameter p with following definition to describe the motion of a photon along its geodesic (Yuan et al. 2009)

$$p = \pm \int^r \frac{dr}{\sqrt{R}} = \pm \int^{\theta} \frac{d\theta}{\sqrt{\Theta_{\theta}}}. \quad (23)$$

Because the sign ahead the integral is the same with dr and $d\theta$, p is always nonnegative and increases monotonically as the photon moves along the geodesic. From the above definition, we know that r and θ are functions of p . In the next section, we will give the explicit forms of these functions by using Weierstrass' and Jacobi's elliptic functions.

3. The expressions of all coordinates as functions of p

3.1. Turning points

From the equations of motion we know that both R and Θ_{θ} must be nonnegative. This restriction divides the coordinate space into allowed (where $R \geq 0$ and $\Theta_{\theta} \geq 0$) and forbidden (where $R < 0$ or $\Theta_{\theta} < 0$) regions for the motion of a photon. The boundary points of these regions are the so called turning points, their coordinates r_{tp} and θ_{tp} satisfy equations $R(r_{tp}) = 0$ and $\Theta_{\theta}(\theta_{tp}) = 0$. For a photon emitted at r_{ini} and θ_{ini} , its motion will be confined between two turning points r_{tp_1} and r_{tp_2} for radial coordinate, θ_{tp_1} and θ_{tp_2} for poloidal coordinate. If we assume $r_{tp_1} \leq r_{tp_2}$, and $\theta_{tp_1} \leq \theta_{tp_2}$, then we have $r_{ini} \in [r_{tp_1}, r_{tp_2}]$ and $\theta_{ini} \in [\theta_{tp_1}, \theta_{tp_2}]$. Because $p_r = \pm \sqrt{R}/\Delta$ and $p_{\theta} = \pm \sqrt{\Theta_{\theta}}$, if $p_r = 0$ (or $p_{\theta} = 0$) at

the initial position, we have $R(r_{ini}) = 0$ (or $\Theta_\theta(\theta_{ini}) = 0$), therefore r_{ini} (or θ_{ini}) must be a turning point and equal to one of r_{tp1} and r_{tp2} (or θ_{tp1} and θ_{tp2}).

The radial motion of a photon can be unbounded, meaning that the photon can go to the infinity or fall into the black hole. These cases usually correspond to equation $R(r) = 0$ has no real roots or r_{tp1} is less or equal to the radius of the event horizon. We regard the infinity and the event horizon of the black hole as two special turning points in the radial motion, a photon will asymptotically approach them but never return from them. Thus r_{tp2} can be the infinity and r_{tp1} can be less or equal to r_h (r_h is the radius of the event horizon).

For the poloidal motion, there is also two special positions, $\theta = 0$ and $\theta = \pi$, i.e., the spin axis of the black hole. A photon with $\lambda = 0$ will go through the spin axis due to zero angular momentum, and will change the sign of its angular velocity $d\theta/d\sigma$ instantaneously, and its azimuthal coordinate will jump from ϕ to $\phi \pm \pi$ (Shakura 1987), implying that the spin axis is not a turning position. From the equation (13) we also know that 0 and π are not the roots of equation $\Theta_\theta(\theta) = 0$.

3.2. μ coordinate

Firstly, we use a new variable μ to replace $\cos \theta$, and the equation (23) can be rewritten as:

$$p = \pm \int^r \frac{dr}{\sqrt{R}} = \pm \int^\mu \frac{d\mu}{\sqrt{\Theta_\mu}}, \quad (24)$$

where

$$\Theta_\mu = q - (q + \lambda^2 - a^2)\mu^2 - a^2\mu^4. \quad (25)$$

Both R and Θ_μ are quartic, but the polynomial of Weierstrass' standard elliptic integral is cubic. We need a variable transformation to make R and Θ_μ to be cubic. We define the following constants for poloidal motion:

$$b_0 = -4a^2\mu_{tp1}^3 - 2(q + \lambda^2 - a^2)\mu_{tp1}, \quad (26)$$

$$b_1 = -2a^2\mu_{tp1}^2 - \frac{1}{3}(q + \lambda^2 - a^2), \quad (27)$$

$$b_2 = -\frac{4}{3}a^2\mu_{tp1}, \quad (28)$$

$$b_3 = -a^2, \quad (29)$$

where $\mu_{tp1} = \cos \theta_{tp1}$ and introduce a new variable t ,

$$t = \frac{b_0}{4} \frac{1}{(\mu - \mu_{tp1})} + \frac{b_1}{4}. \quad (30)$$

Making transformation from μ to t , the μ part of equation (24) can be reduced to

$$p = \pm \int^{t(\mu)} \frac{dt}{\sqrt{4t^3 - g_2t - g_3}}, \quad (31)$$

where $g_2 = \frac{3}{4}(b_1^2 - b_0b_2)$, $g_3 = \frac{1}{16}(3b_0b_1b_2 - 2b_1^3 - b_0^2b_3)$. Using the definition of Weierstrass' elliptic function $\wp(z; g_2, g_3)$ (Abramowitz & Stegun 1965), from equation (31), we have $t = \wp(p \pm \Pi_\mu; g_2, g_3)$. Solving equation (30) for μ , we can express μ as the function of p :

$$\mu(p) = \frac{b_0}{4\wp(p \pm \Pi_\mu; g_2, g_3) - b_1} + \mu_{tp_1}, \quad (32)$$

where

$$\Pi_\mu = |\wp^{-1}[t(\mu_{ini}); g_2, g_3]|. \quad (33)$$

The sign ahead Π_μ depends on the initial value of p_θ , which is the θ component of four momentum of a photon, and

$$\begin{cases} p_\theta > 0, & +, \\ p_\theta = 0, & \begin{cases} \theta_{ini} = \theta_{tp_1}, & \Pi_\mu = n\omega, & +, -, \\ \theta_{ini} = \theta_{tp_2}, & \Pi_\mu = (\frac{1}{2} + n)\omega, & +, -, \end{cases} \\ p_\theta < 0, & -, \end{cases} \quad (34)$$

where ω is the period of $\wp(z; g_2, g_3)$ and $n = 0, 1, 2, \dots$. The sign ahead Π_μ can be "+" or "-" when $p_\theta = 0$.

From the above discussion, we know that one root of equation $\Theta_\mu = 0$ is needed in the variable transformation, namely μ_{tp_1} . To avoid the complexity caused by introducing complex, we always use the real one. Luckily, equation $\Theta_\mu = 0$ always has real roots, but which is not true for equation $R(r) = 0$. For cases in which equation $R(r) = 0$ has no real roots we will use the Jacobi's elliptic functions $\text{sn}(z|k^2), \text{cn}(z|k^2)$ to express r .

3.3. r coordinate

If equation $R(r) = 0$ has real roots, then r_{tp_1} exists, we can define the following constants by using r_{tp_1} :

$$b_0 = 4r_{tp_1}^3 - 2(q + \lambda^2 - a^2)r_{tp_1} + 2[q + (\lambda - a)^2], \quad (35)$$

$$b_1 = 2r_{tp_1}^2 - \frac{1}{3}(q + \lambda^2 - a^2), \quad (36)$$

$$b_2 = \frac{4}{3}r_{tp_1}, \quad (37)$$

$$b_3 = 1, \quad (38)$$

and introduce a new variable t ,

$$t = \frac{b_0}{4} \frac{1}{(r - r_{tp_1})} + \frac{b_1}{4}. \quad (39)$$

It is similar with μ , using t as the independent variable, we can reduce the r part of equation (24) into the standard form of Weierstrass' elliptical integral

$$p = \pm \int^{t(r)} \frac{dt}{\sqrt{4t^3 - g_2t - g_3}}, \quad (40)$$

where $g_2 = \frac{3}{4}(b_1^2 - b_0b_2)$, $g_3 = \frac{1}{16}(3b_0b_1b_2 - 2b_1^3 - b_0^2b_3)$. Taking the inverse of above equation, we get $t = \wp(p \pm \Pi_r; g_2, g_3)$. Solving equation (39) for r , we have

$$r(p) = \frac{b_0}{4\wp(p \pm \Pi_r; g_2, g_3) - b_1} + r_{tp_1}, \quad (41)$$

where

$$\Pi_r = |\wp^{-1}[t(r_{ini}); g_2, g_3]|. \quad (42)$$

The sign ahead Π_r also depends on the initial value of p_r , which is the r component of four momentum of a photon, and

$$\begin{cases} p_r > 0, & +, \\ p_r = 0, & \begin{cases} r_{ini} = r_{tp_1}, & \Pi_r = n\omega, & +, -, \\ r_{ini} = r_{tp_2}, & \Pi_r = (\frac{1}{2} + n)\omega, & +, -, \end{cases} \\ p_r < 0, & -, \end{cases} \quad (43)$$

where ω is the period of $\wp(z; g_2, g_3)$ and $n = 0, 1, 2, \dots$. The sign ahead Π_r can be "+" or "-" when $p_r = 0$.

If equation $R(r) = 0$ has no real roots, we use the Jacobi's elliptic functions to express r . Since the coefficient of r^3 is zero, the roots of equation $R(r) = 0$ satisfy $r_1 + r_2 + r_3 + r_4 = 0$. Therefore the roots r_1, r_2, r_3, r_4 can be written as

$$\begin{aligned} r_1 &= u - iw, & r_2 &= u + iw, \\ r_3 &= -u - iv, & r_4 &= -u + iv. \end{aligned} \quad (44)$$

Introducing two constants λ_1 and λ_2

$$\lambda_{1,2} = \frac{1}{2w^2} [4u^2 + v^2 + w^2 \pm \sqrt{(4u^2 + w^2 + v^2)^2 - 4w^2v^2}], \quad (45)$$

which satisfy $\lambda_1 > 1 > \lambda_2 > 0$, and a new variable t ,

$$t = \sqrt{\frac{\lambda_1 - 1}{(\lambda_1 - \lambda_2)[(r - u)^2 + w^2]}} \left(r - u \frac{\lambda_1 + 1}{\lambda_1 - 1} \right), \quad (46)$$

we can reduce the r part of equation (24) to the Legendre's standard elliptic integral

$$p = \int^t \frac{dt}{w\sqrt{\lambda_1}\sqrt{(1-t^2)(1-m_2t^2)}}, \quad (47)$$

where

$$m_2 = \frac{\lambda_1 - \lambda_2}{\lambda_1}. \quad (48)$$

Using the definition of Jacobi's elliptic function $\text{sn}(z|k^2)$ (Abramowitz & Stegun 1965), from equation (47) we obtain $t = \text{sn}(pw\sqrt{\lambda_1} \pm \Pi_0|m_2)$. Solving the equation (46) for r , we get the expression of r as the function of p

$$r_{\pm}(p) = u + \frac{-2u \pm w(\lambda_1 - \lambda_2)\text{sn}(pw\sqrt{\lambda_1} \pm \Pi_0|m_2)|\text{cn}(pw\sqrt{\lambda_1} \pm \Pi_0|m_2)|}{(\lambda_1 - \lambda_2)\text{sn}^2(pw\sqrt{\lambda_1} \pm \Pi_0|m_2) - (\lambda_1 - 1)}, \quad (49)$$

where

$$\Pi_0 = |\text{sn}^{-1}[t(r_{ini})|m_2]|. \quad (50)$$

When the initial value of $p_r > 0$, we have $r = r_-$, and when $p_r < 0$, we have $r = r_+$. And p_r can not be zero, otherwise the initial radial coordinate r_{ini} of the photon will be one root of equation $R(r) = 0$, which is the case that has been discussed above.

3.4. t and ϕ coordinates and affine parameter σ

In this section, we will express the coordinates t , ϕ and the affine parameter σ as the numerical functions of the parameter p . All of these variables have been expressed as the integrals of r and θ in the equations (9)-(11) and (17)-(22). The goal is achieved if we can compute all of these integrals along a geodesic for a specified p . **Making transformations** from r and μ to a new variable t (defined by equations (30), (39) and (46)), we will compute these integrals under the new variable t . For simplicity we use $F_r(t)$ and $F_\theta(t)$ to denote the complicated integrands (see below) for r and θ respectively.

Firstly, we discuss the integral path, which starts from the initial position and terminates at the photon. If the photon encounters turning points along the geodesic, then the whole integral path is not monotonic, as shown in Figure.1 for poloidal motion (radial motion is similar). In this figure the projected poloidal motion of a photon onto the r - θ plane is illustrated. The motion is confined between two turning points: μ_{tp_1} and μ_{tp_2} . The photon encounters the turning points for three times. Obviously any sections of the path which contain one or more than one turning points is not monotonic, such as path CDE, EFP etc. The path between any two neighboring turning points has the maximum monotonic length and the total integrals should be computed along each of them and summed.

There are four important points involved in the limits of these integrals, i.e., μ_{tp_1} , μ_{tp_2} , μ_{ini} and μ_p , they are the μ coordinates of turning points, initial point and the photon position for a given p respectively. And the values of these points corresponding to the new variable t are t_{tp_1} , t_{tp_2} , t_{ini} , which can be calculated from equation (30), and t_p , which can be calculated from $t = \wp(p \pm \Pi_\mu; g_2, g_3)$ with a given p . Because the function $t = t(\mu)$ expressed by equation (30) is monotonically increasing, we have $t_{tp_2} \leq t_{ini} \leq t_{tp_1}$ and $t_{tp_2} \leq t_p \leq t_{tp_1}$.

If we use Nt_1 and Nt_2 to denote the number of times of a photon meeting the turning points μ_{tp_1} and μ_{tp_2} for a given p respectively, and define the following integrals (cf. Figure 1):

$$\begin{aligned} I_0 &= \int_{t_{ini}}^{t_p} F_\theta(t) dt, & I_1 &= \int_{t_p}^{t_{tp_1}} F_\theta(t) dt, & I_2 &= \int_{t_{tp_2}}^{t_p} F_\theta(t) dt, \\ I_{01} &= I_0 + I_1 = \int_{t_{ini}}^{t_{tp_1}} F_\theta(t) dt, & I_{02} &= I_2 - I_0 = \int_{t_{tp_2}}^{t_{ini}} F_\theta(t) dt, \end{aligned} \quad (51)$$

then the integrals of θ in σ , t and ϕ then can be written as (cf. Figure 1)

$$\begin{aligned} \sigma_\theta (\phi_\theta, t_\theta) &= -\text{sign}(p_\theta)I_0 + 2Nt_1I_1 + 2Nt_2I_2, \\ &= -[\text{sign}(p_\theta) + 2Nt_1 - 2Nt_2]I_0 + 2Nt_1I_{01} + 2Nt_2I_{02}, \end{aligned} \quad (52)$$

where p_θ is the θ component of the initial four momentum of a photon. In order to evaluate the above expression, we need to know Nt_1 and Nt_2 for a given p . Similarly if we define five integrals from the equation (31) as follows:

$$\begin{aligned} p_0 &= \int_{t_{ini}}^{t_p} \frac{dt}{\sqrt{W(t)}}, & p_1 &= \int_{t_p}^{t_{tp_1}} \frac{dt}{\sqrt{W(t)}}, & p_2 &= \int_{t_{tp_2}}^{t_p} \frac{dt}{\sqrt{W(t)}}, \\ p_{01} &= p_0 + p_1 = \int_{t_{ini}}^{t_{tp_1}} \frac{dt}{\sqrt{W(t)}}, & p_{02} &= p_2 - p_0 = \int_{t_{tp_2}}^{t_{ini}} \frac{dt}{\sqrt{W(t)}}, \end{aligned} \quad (53)$$

where $W(t) = 4t^3 - g_2t - g_3$, and we will get the following identity:

$$\begin{aligned} p &= -\text{sign}(p_\theta)p_0 + 2Nt_1p_1 + 2Nt_2p_2, \\ &= -[\text{sign}(p_\theta) + 2Nt_1 - 2Nt_2]p_0 + 2Nt_1p_{01} + 2Nt_2p_{02}. \end{aligned} \quad (54)$$

And notice that Nt_1 and Nt_2 are not arbitrary and related to the initial direction of the photon in poloidal motion. For $p_\theta > 0$ (or $p_\theta = 0$ and $\theta_{ini} = \theta_{tp_1}$), they will increase as

$$\begin{aligned} Nt_1 &= 0 \quad 0 \quad 1 \quad 1 \quad 2 \quad 2 \cdots, \\ Nt_2 &= 0 \quad 1 \quad 1 \quad 2 \quad 2 \quad 3 \cdots. \end{aligned}$$

For $p_\theta < 0$ (or $p_\theta = 0$ and $\theta_{ini} = \theta_{tp_2}$), they will increase as

$$\begin{aligned} Nt_1 &= 0 \quad 1 \quad 1 \quad 2 \quad 2 \quad 3 \cdots, \\ Nt_2 &= 0 \quad 0 \quad 1 \quad 1 \quad 2 \quad 2 \cdots. \end{aligned}$$

For a given p , we find that there always exists one pair of Nt_1 and Nt_2 , which satisfy equation (54) and they are the number of a photon meeting the turning points. With Nt_1 and Nt_2 , the equation (52) now can be evaluated readily.

For r coordinate, the process is similar with the above. Nt_1 and Nt_2 also represent the number of times of a photon meeting the turning points r_{tp_1} and r_{tp_2} respectively. Five integrals are defined as:

$$\begin{aligned} I_0 &= \int_{t_{ini}}^{t_p} F_r(t) dt, \quad I_1 = \int_{t_p}^{t_{tp_1}} F_r(t) dt, \quad I_2 = \int_{t_{tp_2}}^{t_p} F_r(t) dt, \\ I_{01} &= I_0 + I_1 = \int_{t_{ini}}^{t_{tp_1}} F_r(t) dt, \quad I_{02} = I_2 - I_0 = \int_{t_{tp_2}}^{t_{ini}} F_r(t) dt, \end{aligned} \quad (55)$$

where $t_p = \wp(p \pm \Pi_r; g_2, g_3)$ (or $t_p = \text{sn}(pw\sqrt{\lambda_1} \pm \Pi_0|m_2)$ when equation $R(r) = 0$ has no real roots), and t_{p_1} , t_{p_2} and t_{ini} are calculated from equation (39) or (46). Then the integrals of r in σ, t, ϕ can be written as

$$\begin{aligned} \sigma_r (t_r, \phi_r) &= -\text{sign}(p_r)I_0 + 2Nt_1I_1 + 2Nt_2I_2, \\ &= -[\text{sign}(p_r) + 2Nt_1 - 2Nt_2]I_0 + 2Nt_1I_{01} + 2Nt_2I_{02}. \end{aligned} \quad (56)$$

To get Nt_1 and Nt_2 , we define p_0 , p_1 and p_2 from equation (40) as:

$$\begin{aligned} p_0 &= \int_{t_{ini}}^{t_p} \frac{dt}{\sqrt{W(t)}}, \quad p_1 = \int_{t_p}^{t_{tp_1}} \frac{dt}{\sqrt{W(t)}}, \quad p_2 = \int_{t_{tp_2}}^{t_p} \frac{dt}{\sqrt{W(t)}}, \\ p_{01} &= p_0 + p_1 = \int_{t_{ini}}^{t_{tp_1}} \frac{dt}{\sqrt{W(t)}}, \quad p_{02} = p_2 - p_0 = \int_{t_{tp_2}}^{t_{ini}} \frac{dt}{\sqrt{W(t)}}. \end{aligned} \quad (57)$$

For a given p , we have

$$\begin{aligned} p &= -\text{sign}(p_r)p_0 + 2Nt_1p_1 + 2Nt_2p_2, \\ &= -[\text{sign}(p_r) + 2Nt_1 - 2Nt_2]p_0 + 2Nt_1p_{01} + 2Nt_2p_{02}. \end{aligned} \quad (58)$$

To get Nt_1 and Nt_2 from above equation one just needs to notice that when $p_r > 0$ (or $p_r = 0$ and $r_{ini} = r_{tp_1}$) they will increase as

$$\begin{aligned} Nt_1 &= 0 \quad 0 \quad 1 \quad 1 \quad 2 \quad 2 \cdots, \\ Nt_2 &= 0 \quad 1 \quad 1 \quad 2 \quad 2 \quad 3 \cdots, \end{aligned}$$

when $p_r < 0$ (or $p_r = 0$ and $r_{ini} = r_{tp2}$) they will increase as

$$\begin{aligned} Nt_1 &= 0 \quad 1 \quad 1 \quad 2 \quad 2 \quad 3 \cdots, \\ Nt_2 &= 0 \quad 0 \quad 1 \quad 1 \quad 2 \quad 2 \cdots. \end{aligned}$$

Similarly for a given p , there is one pair of Nt_1 and Nt_2 satisfies equation (58). With Nt_1 and Nt_2 equation (56) now can be evaluated. In many cases the number of a photon meeting the turning points in r is less than 2, especially when r_{tp1} is less or equal to r_h , or r_{tp2} is infinity, or equation $R(r) = 0$ has no real roots, both Nt_1 and Nt_2 will be zero.

3.5. Reductions to Carlson's elliptic integrals

In previous sections, four coordinates r, θ, ϕ, t and the affine parameter σ have been expressed as functions of p , and in which many elliptic integrals need to be calculated. In this section, we shall reduce these integrals into standard forms and then evaluate them by Carlson's method as Dexter & Agol (2009) did.

Firstly, we introduce two notations $J_k(h)$ and $I_k(h)$ with following definitions:

$$J_k(h) = \int_{t_1}^{t_2} \frac{dt}{(t-h)^k \sqrt{4t^3 - g_2t - g_3}}, \quad (59)$$

$$I_k(h) = \int_{r_1}^{r_2} \frac{dr}{(r-h)^k \sqrt{(r^2 - 2ur + u^2 + w^2)(r^2 + 2ur + u^2 + v^2)}}, \quad (60)$$

where k is an integer. From equation (8), we get one of the standard forms as

$$J_0 = \int_{t_1}^{t_2} \frac{dt}{\sqrt{4t^3 - g_2t - g_3}}. \quad (61)$$

After being reduced to J_0 , the forms of integrals of r and θ in (8) are exactly same. Noticing the definition of parameter p , we have $J_0 = p$. The radial integrals in equation (9) are reduced to

$$\sigma_r = \frac{b_0^2}{16} J_2\left(\frac{b_1}{4}\right) + \frac{b_0 r_{tp1}}{2} J_1\left(\frac{b_1}{4}\right) + r_{tp1}^2 p, \quad (62)$$

where J_0 has been replaced by p . The radial integrals in equation (10) can be reduced to

$$t_r = \sigma_r + \frac{b_0}{2} J_1\left(\frac{b_1}{4}\right) + (2r_{tp1} + 4 + A_{t+} - A_{t-})p - B_{t+} J_1(t_+) + B_{t-} J_1(t_-), \quad (63)$$

where

$$\begin{aligned}
r_{\pm} &= 1 \pm \sqrt{1 - a^2}, \\
A_{t_{\pm}} &= \frac{2[r_{\pm}(4 - a\lambda) - 2a^2]}{(r_+ - r_-)(r_{tp_1} - r_{\pm})}, \\
B_{t_{\pm}} &= \frac{[r_{\pm}(4 - a\lambda) - 2a^2]b_0}{2(r_+ - r_-)(r_{tp_1} - r_{\pm})^2}, \\
t_{\pm} &= \frac{b_1}{4} + \frac{b_0}{4(r_{\pm} - r_{tp_1})}.
\end{aligned} \tag{64}$$

Similarly the radial integrals in the equation (11) have the following form

$$\phi_r = a[(A_{\phi_+} - A_{\phi_-})p - B_{\phi_+}J_1(t_+) + B_{\phi_-}J_1(t_-)], \tag{65}$$

where

$$\begin{aligned}
A_{\phi_{\pm}} &= \frac{2r_{\pm} - a\lambda}{(r_+ - r_-)(r_{tp_1} - r_{\pm})}, \\
B_{\phi_{\pm}} &= \frac{(2r_{\pm} - a\lambda)b_0}{4(r_+ - r_-)(r_{tp_1} - r_{\pm})^2}.
\end{aligned} \tag{66}$$

When equation $R(r) = 0$ has no real roots, the integrals of r in σ , t and ϕ can be written as:

$$\sigma_r = I_{-2}(0), \tag{67}$$

$$t_r = \sigma_r + 4p + 2I_{-1}(0) + C_{t_+}I_1(r_+) - C_{t_-}I_1(r_-), \tag{68}$$

$$\phi_r = a[C_{\phi_+}I_1(r_+) - C_{\phi_-}I_1(r_-)], \tag{69}$$

where

$$C_{t_{\pm}} = \frac{2[r_{\pm}(4 - a\lambda) - 2a^2]}{r_+ - r_-}, \quad C_{\phi_{\pm}} = \frac{2r_{\pm} - a\lambda}{r_+ - r_-}. \tag{70}$$

The integrals concerning μ in the equation (9) are reduced to

$$\sigma_{\mu} = a^2 \left[\frac{b_0^2}{16} J_2\left(\frac{b_1}{4}\right) + \frac{b_0 \mu_{tp_1}}{2} J_1\left(\frac{b_1}{4}\right) + \mu_{tp_1}^2 p \right], \tag{71}$$

and $t_{\mu} = \sigma_{\mu}$. The μ integrals in the equation (11) can be reduced to

$$\phi_{\mu} = \lambda \left[\frac{p}{1 - \mu_{tp}^2} + W_{\mu_+} J_1(t_+) - W_{\mu_-} J_1(t_-) \right], \tag{72}$$

where

$$\begin{aligned}
W_{\mu_{\pm}} &= \frac{b_0}{8(-1 \pm \mu_{tp_1})^2}, \\
t_{\pm} &= \frac{b_1}{4} + \frac{b_0}{4(\pm 1 - \mu_{tp_1})}.
\end{aligned} \tag{73}$$

Finally we have

$$\begin{aligned}\sigma &= \sigma_r + \sigma_\mu, \\ t &= t_r + t_\mu, \\ \phi &= \phi_r + \phi_\mu.\end{aligned}\tag{74}$$

From equations (61)-(72) we know that the integrals need to be calculated are $J_0, J_1, J_2,$ and I_1, I_{-1}, I_{-2} . Now we use the Carlson's method to evaluate them. When equation $4t^3 - g_2t - g_3=0$ has three real roots denoted by e_1, e_2 and $e_3, J_k(h)$ can be written as (Carlson 1988)

$$\begin{aligned}J_k(h) &= s_h \frac{1}{2} \int_y^x \frac{dt}{\sqrt{(t-e_1)(t-e_2)(t-e_3)(t-h)^{2k}}}, \\ &= s_h \frac{1}{2} [-1, -1, -1, -2k],\end{aligned}\tag{75}$$

where $s_h = \text{sign}[(y-h)^k]$. When equation $4t^3 - g_2t - g_3 = 0$ has one real root e_1 and one pair of complex conjugate roots $u + iv$ and $u - iv, J_k(h)$ can be written as (Carlson 1991)

$$\begin{aligned}J_k(h) &= s_h \frac{1}{2} \int_y^x \frac{dt}{\sqrt{(t-e_1)(t^2 - 2ut + u^2 + v^2)(t-h)^{2k}}}, \\ &= s_h \frac{1}{2} [-1, -1, -1, -2k].\end{aligned}\tag{76}$$

From the equations (30) and (39), we know that when $r = r_{tp_1}$ or $\mu = \mu_{tp_1}, t$ will be ∞ , thus one limit of these integrals can be infinity.

The integrals $I_k(h)$ can be reduced to Carlson's integrals directly (Carlson 1992)

$$\begin{aligned}I_k(h) &= s_h \int_y^x \frac{dr}{\sqrt{(r^2 - 2ur + u^2 + w^2)(r^2 + 2ur + u^2 + v^2)(r-h)^{2k}}}, \\ &= s_h [-1, -1, -1, -1, -2k],\end{aligned}\tag{77}$$

where $[p_1, \dots, p_k]$ is a symbol used by Carlson to denote the elliptic integrals and has the following definition:

$$[p_1, \dots, p_k] = \int_y^x \prod_{i=1}^k (a_i + b_i t)^{p_i/2} dt,\tag{78}$$

which can be evaluated by the formulae provided in Carlson (1988, 1989, 1991, 1992).

4. Constants of motion

4.1. Basic equations

In previous sections we have expressed all coordinates as functions of a parameter p and discussed how to calculate them by Carlson's method. But before the calculation one needs to specify the constants of motion and p_r, p_θ , which determine the signs ahead Π_μ, Π_r, Π_0 and also how the number of turning points increasing. In this section we shall discuss how to compute λ and q and p_r, p_θ from $\bar{p}_{(a)}$, which are the components of the four-momentum measured in the LNRF reference and have been specified by the user.

Firstly, following Bardeen et al. (1972) we introduce the LNRF (locally nonrotating frame) observers or the ZAMO (zero angular momentum observer), the basis vectors of the orthonormal tetrad of them are given by

$$\mathbf{e}_{(a)}(\text{LNRF}) = e_{(a)}^\nu \partial_\nu, \quad (79)$$

where

$$e_{(a)}^\nu = \begin{pmatrix} e^{-\nu} & 0 & 0 & \omega e^{-\nu} \\ 0 & e^{-\mu_1} & 0 & 0 \\ 0 & 0 & e^{-\mu_2} & 0 \\ 0 & 0 & 0 & e^{-\psi} \end{pmatrix}. \quad (80)$$

And the covariant components of the four momentum of a photon in the B-L coordinate can be expressed as

$$p_\mu = E \left(-1, s_r \frac{\sqrt{R}}{\Delta}, s_\theta \sqrt{\Theta_\theta}, \lambda \right), \quad (81)$$

where s_r and s_θ are signs of r and θ components. One can easily show that $\bar{p}_{(a)} = e_{(a)}^\mu p_\mu$, namely (Shakura 1987)

$$\bar{p}_{(t)} = -E e^{-\nu} (1 - \lambda \omega), \quad (82)$$

$$\bar{p}_{(r)} = s_r E e^{-\mu_1} \frac{\sqrt{R}}{\Delta}, \quad (83)$$

$$\bar{p}_{(\theta)} = s_\theta E e^{-\mu_2} \sqrt{\Theta_\theta}, \quad (84)$$

$$\bar{p}_{(\phi)} = E \lambda e^{-\psi}. \quad (85)$$

From equations (83) and (84) we have $s_r = \text{sign}(\bar{p}_{(r)})$ and $s_\theta = \text{sign}(\bar{p}_{(\theta)})$, which determine the initial direction of the photon in the B-L system (cf. equations (34) and (43)), thus determine the way how the number of the turning points increasing.

Solving equations (82) and (85) simultaneously for λ , one obtains

$$\lambda = \frac{\sin \theta \bar{p}_{(\phi)}/\bar{p}_{(t)}}{-\sqrt{\Delta}\Sigma/A + \omega \sin \theta \bar{p}_{(\phi)}/\bar{p}_{(t)}}. \quad (86)$$

Using λ and equation (82), one obtains $E = \bar{p}_{(t)}e^\nu/(1 - \lambda\omega)$. Using λ and E , from equation (84) one obtains the formula of calculating the motion constant q ,

$$q = \left[\left(\frac{\bar{p}_{(\phi)}/\bar{p}_{(t)}}{-\sqrt{\Delta}\Sigma/A + \omega \sin \theta \bar{p}_{(\phi)}/\bar{p}_{(t)}} \right)^2 - a^2 \right] \cos^2 \theta + \left[\frac{\bar{p}_{(\theta)}}{\bar{p}_{(t)}}(1 - \lambda\omega) \right]^2 \frac{A}{\Delta}. \quad (87)$$

Thus we have obtained the basic equations (86) and (87) connecting λ , q and the components of four momentum $\bar{p}_{(a)}$ measured in the LNRF reference. When $\bar{p}_{(a)}$ are given the constants of motion and the initial direction of the photon are both uniquely determined.

To prescribe $\bar{p}_{(a)}$, one should notice that they satisfy following equation

$$-\bar{p}_{(t)}^2 + \bar{p}_{(r)}^2 + \bar{p}_{(\theta)}^2 + \bar{p}_{(\phi)}^2 = 0, \quad (88)$$

thus there are only three independent components. Obviously the user can specify the four momentum $\bar{p}_{(a)}$ directly in LNRF or equivalently specify $p'_{(a)}$ in anyother reference frame of his/her own choice and then to transform it to the LNRF reference by a Lorentz transformation, i.e., $\bar{p}_{(a)} = \alpha_a^{(b)} p'_{(b)}$, where $\alpha_a^{(b)}$ is the transformation matrix. From equations (86) and (87) we know that what one needs is just $\bar{p}_{(i)}/\bar{p}_{(t)}$ and

$$\frac{\bar{p}_{(i)}}{\bar{p}_{(t)}} = \frac{\alpha_i^{(t)} + \alpha_i^{(j)} p'_{(j)}/p'_{(t)}}{\alpha_t^{(t)} + \alpha_t^{(j)} p'_{(j)}/p'_{(t)}}. \quad (89)$$

The $\alpha_a^{(b)}$ should be specified by the user according to his/her needs. ²

As an example, in Figure 2, we show a group of null geodesics emitted isotropically from a particle moving around a black hole in a marginally stable circular orbit (r_{ms}) with

² When a reference frame K' has physical velocities v_r, v_θ, v_ϕ with respect to a LNRF, the general Lorentz transformation matrix has six independent parameters, i.e., $\alpha_a^{(b)} = \alpha_a^{(b)}(\theta_1, \theta_2, \theta_3; v_r, v_\theta, v_\phi)$, where θ_i are the angles between the corresponding spacial basis vectors of the two references. If $\theta_i = 0$, the matrix can be written as follows (Misner et al. 1973)

$$\alpha_a^{(b)} = \begin{pmatrix} \gamma & -\gamma v_r & -\gamma v_\theta & -\gamma v_\phi \\ -\gamma v_r & 1 + \gamma^2 v_r^2/(1 + \gamma) & \gamma^2 v_r v_\theta/(1 + \gamma) & \gamma^2 v_r v_\phi/(1 + \gamma) \\ -\gamma v_\theta & \gamma^2 v_\theta v_r/(1 + \gamma) & 1 + \gamma^2 v_\theta^2/(1 + \gamma) & \gamma^2 v_\theta v_\phi/(1 + \gamma) \\ -\gamma v_\phi & \gamma^2 v_\phi v_r/(1 + \gamma) & \gamma^2 v_\phi v_\theta/(1 + \gamma) & 1 + \gamma^2 v_\phi^2/(1 + \gamma) \end{pmatrix}, \quad (90)$$

$a=0.9375$. And the physical velocities of the particle with respect to the LNRF are $v_r = v_\theta = 0$, $v_\phi = e^{\psi-\nu}(\Omega-\omega)|_{r=r_{ms}}$. The four-momentum $p'_{(a)}$ are specified isotropically in the reference of the particle and then transformed to the LNRF by the Lorentz transformation expressed by equation (90), i.e., $\bar{p}_{(a)} = \alpha_a^{(b)} p'_{(b)}$. With $\bar{p}_{(a)}$ the constants of motion are computed readily. The light bending and beaming effects are illustrated obviously in this figure.

In the next section, we shall discuss how to compute $\bar{p}_{(i)}/\bar{p}_{(t)}$ from impact parameters, which play a key role in imaging. And for simplicity we shall use the transformation expressed by the equations (90) and (91) if the observer has motion.

4.2. Calculation of motion constants from impact parameters

From the works of Cunningham & Bardeen (1973) and Cunningham (1975), we know that λ and q can be calculated from impact parameters, usually denoted by α , β , which are the coordinates of the hitting position of a photon on the photographic plate of the observer. The formulae provided by them read as follows (Cunningham & Bardeen 1973)

$$\lambda = -\alpha \sin \theta_{obs}, \quad (92)$$

$$q = \beta^2 + (\alpha^2 - a^2) \cos^2 \theta_{obs}. \quad (93)$$

The above equations are valid only when the distance between the observer and the emitter is infinite and the observer is stationary. Practically the distance is not infinite, otherwise the integrals of coordinate t will be divergent. When the distance is finite, the above formulae should be modified. We extend those formulae to general situations, in which both the finite distance and the motion state of the observer are considered.

To consider the finite distance is very easy. One just needs to substitute the coordinates r_{obs}, θ_{obs} of the observer into equations (86) and (87) in the calculation. While to consider the motion state is more complicated. Obviously we can distinguish the motion states of the observer into two kinds. In the first one the observer is stationary and in the second one the observer has physical velocities v_r, v_θ, v_ϕ with respect to the LNRF reference.

where $\gamma = [1 - (v_r^2 + v_\theta^2 + v_\phi^2)]^{-1/2}$, and its inverse form

$$\tilde{\alpha}_{(a)}^b = \begin{pmatrix} \gamma & \gamma v_r & \gamma v_\theta & \gamma v_\phi \\ \gamma v_r & 1 + \gamma^2 v_r^2 / (1 + \gamma) & \gamma^2 v_r v_\theta / (1 + \gamma) & \gamma^2 v_r v_\phi / (1 + \gamma) \\ \gamma v_\theta & \gamma^2 v_\theta v_r / (1 + \gamma) & 1 + \gamma^2 v_\theta^2 / (1 + \gamma) & \gamma^2 v_\theta v_\phi / (1 + \gamma) \\ \gamma v_\phi & \gamma^2 v_\phi v_r / (1 + \gamma) & \gamma^2 v_\phi v_\theta / (1 + \gamma) & 1 + \gamma^2 v_\phi^2 / (1 + \gamma) \end{pmatrix}. \quad (91)$$

In the first kind, the observer is just a LNRF observer and whose orthonormal tetrad is given by equation (79), namely $\mathbf{e}_{(a)}(\text{obs}) = \mathbf{e}_{(a)}(\text{LNRF})$. While in the second kind, the tetrad of the observer can be created by a Lorentz transformation, i.e., $\mathbf{e}_{(a)}(\text{obs}) = \tilde{\alpha}_{(a)}^b \mathbf{e}_{(b)}(\text{LNRF})$. Here $\tilde{\alpha}_{(a)}^b$ is given by the equation (91).

As shown in Figure 3, we plot the image of a photon hitting on the photographic plate. The plate is located in the plane determined by the basis vectors $\mathbf{e}_{(\theta)}(\text{obs})$ and $\mathbf{e}_{(\phi)}(\text{obs})$, and in which an orthonormal coordinate system α, β has been established. The basis vectors \mathbf{e}_α and \mathbf{e}_β of the system are aligned with $\mathbf{e}_{(\phi)}(\text{obs})$ and $\mathbf{e}_{(\theta)}(\text{obs})$ respectively. All photons will go through the center of the Lens before hitting on the plate. From this figure, one obtains the relationships between the impact parameters and $p'_{(a)}$ as follows:

$$\alpha = r scal \left. \frac{p'_{(\phi)}}{p'_{(r)}} \right|_{r=r_{obs}, \theta=\theta_{obs}}, \quad (94)$$

$$\beta = r scal \left. \frac{p'_{(\theta)}}{p'_{(r)}} \right|_{r=r_{obs}, \theta=\theta_{obs}}. \quad (95)$$

And obviously one can read off $p'_{(r)} > 0$, $\alpha p'_{(\phi)} \geq 0$ and $\beta p'_{(\theta)} \geq 0$.

Two dimensionless factors r and $scal$ have been multiplied to amplify the size of the image, otherwise which will be infinite small, since the distance D between the central compact object and the observer and the size of the target object L satisfy $D \gg L$.

In the rest frame of the observer, the spacetime is locally flat, we still have

$$-p'^2_{(t)} + p'^2_{(r)} + p'^2_{(\theta)} + p'^2_{(\phi)} = 0. \quad (96)$$

Using equations (94), (95) and (96) and noting the signs of $p'_{(a)}$, α, β , we obtain

$$\frac{p'_{(r)}}{p'_{(t)}} = -\frac{1}{\sqrt{1 + (\alpha/r scal)^2 + (\beta/r scal)^2}}, \quad (97)$$

$$\frac{p'_{(\theta)}}{p'_{(t)}} = -\frac{\beta/r scal}{\sqrt{1 + (\alpha/r scal)^2 + (\beta/r scal)^2}}, \quad (98)$$

$$\frac{p'_{(\phi)}}{p'_{(t)}} = -\frac{\alpha/r scal}{\sqrt{1 + (\alpha/r scal)^2 + (\beta/r scal)^2}}. \quad (99)$$

Substituting equations (97)-(99) into (89), we get the functions $\bar{p}_{(i)}(\alpha, \beta)/\bar{p}_{(t)}(\alpha, \beta)$. We can then calculate λ and q from impact parameters by using equations (86) and (87).

One can verify directly that when $r_{obs} \rightarrow \infty$, $scal = 1$, and $v_r = v_\theta = v_\phi = 0$, the equations (86) and (87) reduce to (92) and (93) immediately.

If the observer has motion, the image on the plate will have a displacement compare to the image when the observer is stationary. The displacement is proportional to the observer's velocity and can be described by α_c, β_c , which is the coordinates of image point of the origin of B-L coordinate system on the photographic plate. Obviously α_c and β_c satisfy the following equations:

$$\bar{p}_{(\theta)}(\alpha_c, \beta_c) = 0, \quad (100)$$

$$\bar{p}_{(\phi)}(\alpha_c, \beta_c) = 0. \quad (101)$$

Actually, $\bar{p}_{(\phi)}(\alpha, \beta) = 0$ represents the projection of the spin axis of the black hole onto the plate. When $v_r = v_\theta = v_\phi = 0$, the above equations become $\alpha_c = 0$ and $\beta_c = 0$. The region of the image on the plate therefore is $[-\Delta L + \alpha_c, \Delta L + \alpha_c]$ and $[-\Delta L + \beta_c, \Delta L + \beta_c]$, where ΔL is the half length of the image.

4.3. Redshift formula

The redshift g of a photon is defined by $g = E_{obs}/E_{em}$. From above discussion, we know that $E_{obs} = -p'_{(t)}$, $E_{em} = -p_\mu u^\mu_{em}$, where u^μ_{em} is the four-velocity of the emitter. If we define

$$f_t = \alpha_t^{(t)} + \alpha_t^{(i)} \frac{p'_{(i)}}{p'_{(t)}}. \quad (102)$$

From equation (82), we have $-p'_t = Ee^{-\nu}(1 - \lambda\omega)/f_t$. Using the equation (81), then g can be expressed as follows

$$g = \frac{[e^{-\nu}(1 - \lambda\omega)/f_t]_{obs}}{\left[u^t \left(1 + s_r \dot{r} \sqrt{R}/\Delta + s_\theta \dot{\theta} \sqrt{\Theta_\theta} - \lambda\Omega \right) \right]_{em}}, \quad (103)$$

where $\dot{r} = u^r/u^t$, $\dot{\theta} = u^\theta/u^t$, $\Omega = \dot{\phi} = u^\phi/u^t$ are the coordinate velocities.

With $\dot{r}, \dot{\theta}, \Omega$, the physical velocities of the emitter with respect to the LNRF v_r, v_θ, v_ϕ can be written as (Bardeen et al. 1972)

$$v_r = e^{\mu_1 - \nu} \dot{r}, \quad v_\theta = e^{\mu_2 - \nu} \dot{\theta}, \quad v_\phi = e^{\psi - \nu} (\Omega - \omega), \quad (104)$$

with which the four-velocity of the emitter can be expressed as

$$u^\mu_{em} = \gamma(e^{-\nu}, v_r e^{-\mu_1}, v_\theta e^{-\mu_2}, \Omega e^{-\nu}). \quad (105)$$

Then the g can be rewritten as (Müller & Camenzind 2004)

$$g = \frac{[e^{-\nu}(1 - \lambda\omega)/f_t]_{obs}}{\left[\gamma e^{-\nu} \left(1 + s_r e^{\nu} v_r \sqrt{R}/\sqrt{\Sigma\Delta} + s_\theta e^{\nu} v_\theta \sqrt{\Theta_\theta}/\sqrt{\Sigma} - \lambda\Omega\right)\right]_{em}}. \quad (106)$$

For an emitter moving in a Keplerian orbit, the formula of g reduces to

$$g = \frac{[e^{-\nu}(1 - \lambda\omega)/f_t]_{obs}}{[\gamma e^{-\nu} (1 - \lambda\Omega)]_{em}}. \quad (107)$$

5. A brief introduction to the code

5.1. The four coordinates and affine parameter functions

We have expressed the four coordinates r , μ , ϕ , t and the affine parameters σ as functions of p . We denote them as follows:

$$r(p), \mu(p), \phi(p), t(p), \sigma(p). \quad (108)$$

In practical applications, we are interested in determining the original position where the photon was emitted or the regions traveled by the photon. To make the calculations effectively, all photons are traced backward from the observer to the emitter along the geodesics. But not all photons start from the observer will go through the emission region one interested, and the tracing process will be terminated either these photons go to the infinity or fall into the event horizon of a black hole.

Now we discuss how to determine the intersection of a geodesic with the surface of an optically thick emission region, we assuming that the optical depth of which is so large that a sharply emission surface exists. And the surface is smooth and continuous and can be described by an algebra equation:

$$F(r, \theta, \phi) = F_0, \quad \text{or} \quad F(x, y, z) = F_0, \quad (109)$$

where x , y , z are the pseudo Cartesian coordinates and defined by

$$x = \sqrt{r^2 + a^2} \sin \theta \cos \phi, \quad y = \sqrt{r^2 + a^2} \sin \theta \sin \phi, \quad z = r \cos \theta. \quad (110)$$

In some special cases the surface one considered may not keep stationary, the surface equation will be a function of time t , i.e., $F(r, \theta, \phi, t) = F_0$. We introduce a function $f(p)$ defined by

$$f(p) = F[r(p), \theta(p), \phi(p)] - F_0. \quad (111)$$

Then the roots of equation $f(p) = 0$ correspond to the intersections of the geodesic with the target surface. Therefore if equation $f(p) = 0$ has no roots, the geodesic will never intersect with the surface. To solve this equation effectively, we classify geodesics into four classes denoted by A, B, C and D, according to their relationships with respect to a shell, shown in Figure 5. The shell includes the emission region completely, and its inner and outer radius are r_{in} and r_{out} . Reminding that r_{tp_1} and r_{tp_2} are turning points, between which the radial motion of a photon is confined. Geodesics in the four classes satisfy the conditions A: $r_{tp_1} > r_{out}$, B: $r_{in} \leq r_{tp_1} \leq r_{out}$, C: $r_h < r_{tp_1} < r_{in}$ and D: $r_{tp_1} \leq r_h$ respectively, where r_h is the radius of the event horizon.

The values of parameter p corresponding to the intersections of the geodesic with the shell are denoted by p_1, p_2, p_3, p_4 , which satisfy $p_1 < p_2 < p_3 < p_4$. Obviously the roots of equation $f(p) = 0$ may exist on intervals $[p_1, p_2]$ and $[p_3, p_4]$. We use the Bisection or the Newton-Raphson method to search the roots (Press et al. 2007).

Solving the radiative transfer equation in optically thin or thick media, one needs to evaluate integrations along geodesic with taking the affine parameter σ as the independent variable. Since we have taken p to be the independent variable, we can replace σ by p to evaluate these integrals. From the definition of p , i.e., equation (23), one has

$$dp = \pm \frac{dr}{\sqrt{R(r)}} = \pm \frac{d\theta}{\sqrt{\Theta_\theta}}, \quad (112)$$

and from the equations (4) and (5) one gets

$$d\sigma = \pm \Sigma \frac{dr}{\sqrt{R(r)}} = \pm \Sigma \frac{d\theta}{\sqrt{\Theta_\theta}}. \quad (113)$$

From above equations one immediately obtains

$$d\sigma = \Sigma dp, \quad (114)$$

which converts the independent variable from σ to p in radiative transfer applications (Yuan et al. 2009).

Finally we give a brief discussion on the determination of a geodesic connecting the emitter and observer (Viergutz 1993; Beckwith & Done 2005). We use α_{em}, β_{em} to represent the impact parameters of the geodesic which connecting the observer and emitter and p_{em} to indicate the position of the emitter on the geodesic, in which the coordinates of the emitter are r_{em}, μ_{em} and ϕ_{em} . Obviously we have the following set of equations:

$$r(p_{em}, \alpha_{em}, \beta_{em}) = r_{em}, \quad (115)$$

$$\mu(p_{em}, \alpha_{em}, \beta_{em}) = \mu_{em}, \quad (116)$$

$$\phi(p_{em}, \alpha_{em}, \beta_{em}) = \phi_{em}. \quad (117)$$

In principle if we can solve this set of nonlinear equations simultaneously for $p_{em}, \alpha_{em}, \beta_{em}$, the geodesic is determined uniquely. Therefore the observer-emitter problem also becomes a root finding problem. In our code we use the Newton-Raphson method (Press et al. 2007) to solve these equations.

5.2. The code

In this section we shall give a brief introduction for the code, and a more detailed introduction is given in the README³ file. The code is named YNOGK (Yun-Nan Observatory Geodesics Kerr) and written by Fortran 95, in which the object-oriented method has been used. The code is composed by a couple of modules. For each module, a special function has been implemented and one can use all supporting functions and subroutines in that module by a command "use module-name" in his/her own program. By adding corresponding modules into one's own code, one can easily develop new ones to handle special and more sophisticated applications.

Two modules named **ell-function** and **BLcoordinate** are the most important ones in ynogk, the former one includes supporting functions and subroutines for calculating the Carlson's elliptic integrals and the R-functions. Many routines in this module come from geokerr (Dexter & Agol 2009) and Numerical recipes (Press et al. 2007). The latter module includes routines for computing all coordinates and the affine parameter functions: $t(p), r(p), \theta(p), \phi(p)$ and $\sigma(p)$. To call these routines, constants of motion and components of four-momentum $\bar{p}_{(r)}, \bar{p}_{(\theta)}, \bar{p}_{(\phi)}$ measured in a LNRF reference must be prescribed, which can be computed by two subroutines named **lambdaq** and **initialdirection** in ynogk. The former routine computes the constants of motion from impact parameters, while the latter one computes λ and q from the initial $p'_{(a)}$ given in a reference K' , which has physical velocities v_r, v_θ, v_ϕ with respect to the LNRF. Of course one can compute them by his/her own subroutines according to their needs. According to the discussion in Section 5.1, we present a module named **pem-finding** to search the minimum root p_{em} of equation $f(p) = 0$, and $f(p)$ as an external function should be given by the user. In module **obs-emitter**, we present routines to find the root of equations (115)-(117) by using the Newton-Raphson algorithm (Press et al. 2007). In the testing section of the code, this module has been used to determine the geodesic connecting the observer and the central point of a hot spot, which movies in the inner most stable circular orbit (ISCO). With the geodesic the motion of the spot can be described easily. The results are agree very well with previous works, in which a very

³<http://www1.ynao.ac.cn/~yangx1/readme.pdf>

different method has been used to determine the motion of the spot, i.e., by tabulating the motion according to the time of the observer over one period (Schnittman & Bertschinger 2004; Dexter & Agol 2009).

All routines for computing the Carlson’s elliptic integrals have been extensively checked by NIntegrate function of Mathematica. The original code of these routines comes from geokerr (Dexter & Agol 2009), and has been modified to adapt to our code. The original code for the computing of R-functions comes from Numerical recipes (Press et al. 2007). The same check also has been done for the functions $t(p), r(p), \theta(p), \phi(p), \sigma(p)$. When $|\alpha|$ and $|\beta| \lesssim 10^{-7}$, we let them to be zero, since the Carlson’s integrals can not maintain their accuracy. The treatment is same for any other parameters if they take offending values. For some critical cases, special treatments also have been implemented.

5.3. Comparisons and speed tests

Our code has many common points with geokerr of Dexter & Agol (2009). We both use the Carlson’s method to compute the elliptic integrals and use the elliptic functions to express all coordinates as functions of a independent variable. But the elliptic functions we used are mainly the Weierstrass’ elliptic function $\wp(z; g_2, g_3)$, which has a cubic polynomial, leading simpler root distribution and the cases of integral are reduced. In our code the four B-L coordinates r, θ, ϕ, t and affine parameter σ are expressed as analytical or numerical functions of a parameter p , which corresponds to I_u or I_μ in Dexter & Agol (2009). With this treatment one can compute the geodesics directly without providing any information about the turning points in advance. Which also allows one to track emissions from a more sophisticated surface, not only for standard thin accretion disk. In the code testing section we will show the images of a warped disk, which has a curved surface.

Our strategy, i.e., expressing coordinates as functions of p semi-analytically, can be extended to compute the timelike geodesics directly, almost without any modifications. As mentioned in Dexter & Agol (2009), the calculations of the timelike geodesics involve many more cases. The main challenge is to specify the number of radial turning points for bounded orbits in advance. But our strategy does not require the specification of the number of turning points both in radial and poloidal coordinates in advance, therefore which can be used naturally and effectively in the calculations of timelike geodesics even in a Kerr-Newmann spacetime.

In our code we give the orthenormal tetrad of the emitter or the observer analytically, provided the physical velocities of which with respect to the LNRF are specified. They

may be useful in Monte-Carlo type code of radiative transfer, which needs one to make transformations from the reference of the emitter to the B-L coordinate system frequently (Dolence et al. 2009). As illustrated in figure 2, emissions in the reference of the emitter are specified isotropically, but from the perspective of the B-L coordinate system which are anisotropic due to the Doppler beaming effect.

Our testing results for various toy problems agree well with those of Dexter & Agol (2009). In Figure 4 we illustrate the projection of a uniform orthonormal grid from the photographic plate of the observer onto the equatorial plane of a black hole, in which the solid and dotted lines represent the results from our code and geokerr respectively. They agree with each other very well.

The basic strategy used in ynogk to compute the elliptic integrals and functions are very similar to geokerr. For example we make ynogk to compute the minimum number of R-functions possible and share them between routines. This strategy improves the speed of our code greatly. But there is still some differences between the two codes. Firstly, we assemble $r(p)$ and $\mu(p)$ into routines for computing $t(p)$, $\phi(p)$ and $\sigma(p)$, thus the repeated calculations for the same integrals among those functions can be avoided. We provide a routine named **ynogk** to compute the four B-L coordinates and affine parameter simultaneously. We also provide two independent routines named **radius** and **mucos** to compute $r(p)$ and $\mu(p)$ respectively. Secondly, ynogk can save the values of variables used in the calculations for a same geodesic but for different p . These values can be used repeatedly.

ynogk has almost same speed with the geokerr in tracing radiations from an optically and geometrical thin disk, because there is only one point, i.e., the intersection of the ray with the disk surface, needs to be calculated. For the calculations of radiative transfer, in which many points are needed along each geodesics, ynogk has a little slower than geokerr. The speed tests of a code are not only dependent on the applications mostly, but also on the environment of the code running. From the testing results of ynogk, we expect that the speed of which is almost same with geokerr in many other applications.

For more detailed introductions, one can see the README file. In the next section, we will show the testing results of our code for toy problems.

6. The tests of our code

In this section, we shall present the testing results of our code for toy problems. The results not only demonstrate the validation our code, but also give specific examples of its utility. Firstly, we show the image of a black hole shadow, in which the intensity represents

the value of the affine parameter σ . By this example we want to test the validation of function $\sigma(p)$. Then we show the images of a couple of accretion disks and a rotationally supported torus, all of them are optically thick and have a sharply emission surface. The disks include the standard thin, thick and warped disks. Next we show the images of a ball orbiting around a Kerr black hole in a Keplerian orbit to illustrate the gravitational lensing effect. Then we calculate the line profiles of the Fe $K\alpha$ and the blackbody radiation spectra of a standard thin accretion disk around a Kerr black hole. In order to test the accuracy of function $t(p)$, we image a hot spot moving around a Kerr black hole in the ISCO for various black hole spins. We also calculate the spectrogram and light curves of the spot over one period of the motion with various inclinations for a Schwarzschild black hole. Finally we discuss the radiative transfer equation and its solution, which the radiative transfer process in a radiation dominated torus around a black hole has been discussed. We give the images of the torus for optically thin and thick cases. The resolution of images in this section is taken to be 801×801 , each pixel corresponds to an unique geodesic.

6.1. Black hole shadow

As the first test of our code we give the image of a black hole shadow. We trace all photons backward from the photographic plate to the black hole along geodesics. The intensities of the image are taken to be the affine parameter σ evaluated from the observer to terminations on the geodesic—either when it intersects with the event horizon of the black hole or reaches a turning point and returns to the starting radius. The evaluations of the affine parameter outside the shadow are multiplied a factor 1/2. In Figure 6, we show the image from an edge-on view. We take the spin a to be 0.998, and the distance of the observer to be $10^6 r_g$, where r_g is the gravitational radius.

To evaluate affine parameter σ from function $\sigma(p)$, we need p_h , which is the value of parameter p corresponds to the event horizon and also the root of equation $r(p) = r_h$. We can get p_h by evaluating the integral of r in the definition of p , and need not to solve this equation directly. We provide a routine named **r2p** to complete this evaluation.

6.2. Accretion disks

Next we present the images of the accretion disks around a Kerr black hole, including the standard thin, thick and warped disks. The imaging of the disks is usually taken as the first step to calculate the line profiles of the Fe $K\alpha$ and the spectrum (Li et al. 2005).

Usually the pseudo colors of the image represent the redshift g or the observed flux intensity I_ν of emissions come from the disk.

In Figure 7, we show the image of a standard thin disk, the inner and outer radius of which is r_{ms} and $22 r_g$ respectively. The black hole spin a is 0.998 and the inclination angle θ_{obs} is 86° . The distance of the observer is $40 r_g$. The shape of the image is quite different from the one observed from infinite far away. We also illustrate the high-order images of the disk in this figure. Due to the light bending and focusing, one can see the part behind the black hole and the bottom side of the disk. The color intensities represent the redshift g of emissions come from the disk.

In order determine the intersections of geodesics with the disk, we need to know the minimum root of equation $\mu(p) = 0$. We provide two routines named **pemdisk** and **pemdisk-all** to compute the root by evaluating the integral of μ in the definition of p . Using **pemdisk** one can draw the direct image, while using **pemdisk-all** one can draw the direct and high-order images.

The surface of the thick disk has a constant inclination angle δ with respect to the equatorial plane (Wu & Wang 2007). To trace the thick disk, we need to solve equation $\mu(p) = \cos(\pi/2 - \delta)$ to get p for the upper surface and $\mu(p) = \cos(\pi/2 + \delta)$ for the bottom surface, the roots of these two equations can also be computed by **pemdisk** and **pemdisk-all**. Since the surface particles of the disk no longer keep in the equatorial plane, they will do the sub-Keplerian motion with a angular velocity given by (Ruszkowski & Fabian 2000)

$$\Omega = \left(\frac{\theta}{\pi/2} \right)^{\frac{1}{n}} \Omega_K + \left[1 - \left(\frac{\theta}{\pi/2} \right)^{\frac{1}{n}} \right] \omega, \quad (118)$$

where $\Omega_K = 1/(r^{3/2} + a)$ is the Keplerian velocity and parameter n is taken to be 3 here. Using the equation (107), we can calculate the redshift of the emissions come from the disk. The images are shown in Figure 8, which agrees very well with Figure 10 of Wu & Wang (2007).

The warped accretion disk is also a very interesting object in astrophysics (Bardeen & Petterson 1972; Wu & Wang 2007; Wang & Li 2012). Here we discuss a very simple model for the warped disk, in which the disk is assumed to be optically thick and its surface can be described by (Wang & Li 2012)

$$\cot \theta = -\tan \beta \cos(\phi - \gamma), \quad (119)$$

where parameters γ and β are defined by

$$\gamma(p) = \gamma_0 + n_1 \exp \left[n_2 \frac{r_{in} - r(p)}{r_{out} - r_{in}} \right], \quad (120)$$

$$\beta(p) = n_3 \sin \left[\frac{\pi}{2} \frac{r(p) - r_{in}}{r_{out} - r_{in}} \right], \quad (121)$$

where r_{in} and r_{out} are the inner and outer radius of the disk, and n_1, n_2, n_3 are the warping parameters. With above equations, we get the $f(p)$ as follows

$$f(p) = \tan \beta(p) \cos[\phi(p) - \gamma(p)] + \frac{\mu(p)}{\sqrt{1 - \mu^2(p)}}. \quad (122)$$

With the minimum root of equation $f(p) = 0$, we can image the warped disk. For the poloidal velocity $\dot{\theta}$ of the particle is nonzero, the formula (103) or (106) is used to calculate the redshift g (cf. Wang & Li (2012)). The images of the warped disk are shown in Figure 9, in which the warping parameters n_1 and n_2 are nonzero, leading the disk warps along azimuthal direction. For comparison one can see Figure 3 of Wang & Li (2012), in which n_1 is taken to be zero for simplicity, thus the shape of the disk is quite different from the one illustrated here.

6.3. Rotationally supported torus

In this section, we give the images of a rotationally supported torus. For simplicity we give a brief introduction for the torus model here, for the more detailed discussions one is recommended to the paper of Fuerst & Wu (2004) or Younsi et al. (2012). The torus is assumed to be stationary and axisymmetric. Due to the balance of the centrifugal force, gravity and pressure force, the structure of the torus is stratified and the isobaric surfaces can be described by a set of differential equations (Younsi et al. 2012)

$$\frac{dr}{d\zeta} = \frac{\psi_2}{\sqrt{\psi_2^2 + \Delta\psi_1^2}}, \quad (123)$$

$$\frac{d\theta}{d\zeta} = \frac{-\psi_1}{\sqrt{\psi_2^2 + \Delta\psi_1^2}}, \quad (124)$$

where

$$\psi_1 = M \left(\frac{\Sigma - 2r^2}{\Sigma^2} \right) (\Omega^{-1} - a \sin \theta)^2 + r \sin^2 \theta, \quad (125)$$

$$\psi_2 = \sin 2\theta \left(\frac{Mr}{\Sigma^2} [a\Omega^{-1} - (r^2 + a^2)]^2 + \frac{\Delta}{2} \right), \quad (126)$$

$$\Omega = \frac{\sqrt{M}}{(r \sin \theta)^{3/2} + a\sqrt{M}} \left(\frac{r_k}{r \sin \theta} \right)^n, \quad (127)$$

and Ω is the angular velocity. r_k represents the radius at which the the particle orbits with a Keplerian velocity. The index parameter n is crucial for regulating the angular velocity profile and adjusting the geometrical aspect ratio of the torus. ζ is an auxiliary parameter. In order to give the outer surface of the torus, one needs to specify the most inner radius of the torus, which is usually regarded as the intersection of the isobaric surface with the ISCO. Taking the inner most radius in the equatorial plane to be the initial condition, the differential equations (123) and (124) are now readily to be integrated. In Figure 10 we illustrate the images of the torus, which has the same parameters with Figure 3 of Younsi et al. (2012), the results agree with each other very well.

6.4. The gravitational lensing effect

Due to the strong gravity field, when the trajectory of a photon is closed to the vicinity of a compact object, it will be bent or focused, then multiple images will be observed, this is the so called gravitational lensing effect. Here this phenomenon will be illustrated by a simple example, in which a ball moves around a near extremal black hole ($a=0.998$) in a Keplerian orbit. The radius of the orbit is R_0 , then the angular velocity of the ball is $\Omega = 1/(R_0^{3/2} + a)$. The coordinates of the center of the ball will be

$$x_0(p) = \sqrt{R_0^2 + a^2} \cos[\Omega t(p)], \quad (128)$$

$$y_0(p) = \sqrt{R_0^2 + a^2} \sin[\Omega t(p)], \quad (129)$$

$$z_0(p) = 0. \quad (130)$$

Then the function of the surface of the ball can be expressed as follows:

$$f(p) = \sqrt{[x(p) - x_0(p)]^2 + [y(p) - y_0(p)]^2 + z(p)^2} - r_1, \quad (131)$$

where r_1 is the radius of the ball. The images observed from an edge-on view are illustrated in Figure 11. For different positions of the ball in its orbit, the image changes greatly, which even becomes a ring as the ball movies to the back of the even horizon.

6.5. The line profiles of Fe $K\alpha$

The calculation of line profiles is very easy provided the structure of the disk is specified. For simplicity, we assume that the particles of the accretion flow do the Keplerian motion and the disk is geometrical thin and optically thick. The inner and outer radius of the disk

are located at r_{ms} and $15 r_g$ respectively. The emission is monochromatic and the profile of which can be described by the Dirac's δ function in the local rest frame of the flow

$$I_{em}(\nu) = \frac{\epsilon_0}{4\pi r^n} \delta(\nu - \nu_{em}), \quad (132)$$

where n is the index of emissivity and assumed to be 3. Since I_ν/ν^3 is an invariance along a geodesic (Misner et al. 1973), we get the observed intensity $I_{obs} = g^3 I_{em}$, where $g = \nu_{obs}/\nu_{em}$ is the redshift. Then the observed flux density F_ν at frequency ν can be computed by integrating I_{obs} over the whole plate as following expression

$$F_\nu = \int \frac{\epsilon_0}{4\pi r^n} \delta(\nu - \nu_{em}) g^3 d\alpha d\beta. \quad (133)$$

The observed intensities have been normalized in the computation. The results are shown in Figure 12, which agrees very well with the Figure 3 of Čadež et al. (1998). From this figure one can see that the higher black hole spin leads the broadening in low frequency for the ISCO is closer to the event horizon, the gravitational redshift effect is remarkable, while the higher inclination angle leads the broadening in high frequency for the Doppler beaming effect.

6.6. The blackbody radiation spectrum of a Keplerian disk

In this section we will compute the spectrum of a Keplerian disk around a Kerr black hole to illustrate effects of the black hole spin and the observer's inclination angles on the observed profiles of the spectrum (Li et al. 2005). Similarly, the disk is assumed to be geometrical thin and optically thick, and the radiation spectrum of the disk in its local rest frame is an isotropic blackbody spectrum. We denote the effective temperature of the disk by T_{eff} . Then radiation intensity at frequency ν can be written as

$$I_{em}(\nu) = \frac{h\nu^3}{\exp(h\nu/k_B T_{\text{eff}}) - 1}, \quad (134)$$

where h and k_B are the Plank and Boltzmann constants respectively. For a blackbody radiation, the effective temperature is simply

$$T_{\text{eff}} = \left[\frac{F(r)}{\sigma_{SB}} \right]^{1/4}, \quad (135)$$

where σ_{SB} is the Stefan-Boltzmann constant. Here we do not consider effect of the returning radiation of the disk on the spectrum, therefore $F(r)$ is just the energy flux emitted from the disk's surface measured by a locally corotating observer. For the Keplerian accretion

disk around a Kerr black hole, Page & Thorne (1974) have get the analytical expression for $F(r)$, i.e.,

$$F(r) = \frac{\dot{M}}{4\pi r} f, \quad (136)$$

where \dot{M} is mass accretion rate, f is a function of r, a, r_{ms} , and the seminal expression of which is given by equations (15d) and (15n) of Page & Thorne (1974). With $F(r)$ the effective temperature of the disk can be computed readily. Using the invariance I_ν/ν^3 , one can get the observed intensity $I_{obs} = g^3 I_{em}$. The total observed flux density at frequency ν therefore is the integration of I_{obs} over the whole plate

$$F(\nu_{obs}) = \int \frac{h\nu_{obs}^3}{\exp(h\nu_{obs}/gk_B T_{eff}) - 1} d\alpha d\beta. \quad (137)$$

Then the photon number flux density is $N_{obs} = F(\nu_{obs})/E_{obs}$.

The results are plotted in Figure 13. Compare to the Figure 5 of Li et al. (2005) we find that the basic features of the two figures are in agreement. For example, as shown in top panel, we see that as the spin of the black hole goes up the spectrum becomes harder. Physically, this is due to the fact that as the spin a increases, the system of the accretion disk has a higher radiation efficiency and a higher temperature. In the bottom panel of Figure 13, we can see that at the low-energy end, the flux density goes down as θ_{obs} goes up. As explained by Li et al. (2005) this is caused by the projection effect. While at the high-energy end, the flux density goes up as the θ_{obs} increases. As pointed out by Li et al. (2005) this is resulted from the joint action of the effects of Doppler beaming and gravitational focusing.

In the top panel there is a noticeable effect: even though we do not consider the returning radiation, the flux density goes up as the spin increases in the low-energy end. Li et al. (2005) suggested that this effect is caused by the returning radiation. We proposal that this explanation may be not correct and the effect is just caused by the simple fact that a higher spin leads to a higher radiation efficiency and temperature.

6.7. The motion of a hot spot

In order to test the validation of the function $t(p)$ and illustrate the time delay effect in the Kerr spacetime, we image a hot spot orbiting around a black hole retrogradely in a marginally stable circular orbit for various spins and compute the observed light curve and spectra. The radius of the spot is $R_{spot}=0.5 r_g$. The emissivity of the spot is taken to be

Gaussian shape in its rest frame (Schnittman & Bertschinger 2004), i.e.,

$$j(\mathbf{x}) \propto \exp \left[-\frac{|\mathbf{x} - \mathbf{x}_{\text{spot}}(t)|^2}{2R_{\text{spot}}^2} \right]. \quad (138)$$

For the motion of the spot, one must consider the time delay effect and the azimuthal position of the spot when imaging the spot and calculating its spectra. In order to compute the time delay Δt for each geodesic starting from the photographic plate, a reference time t_{obs} , which is taken to be the time used by a photon traveling from the central point of the spot to the observer, needs to be specified. Meanwhile the position of the spot can be determined by its central coordinates $(r_{ms}, \mu = 0, \phi_{\text{spot}})$. Then with the method discussed in section 5, (i.e., the method to determine a geodesic connecting the observer and emitter with the given coordinates), we can determine the geodesic connecting the central point of the spot and the observer. With this geodesic the reference time t_{obs} can be calculated readily. Using t_{obs} , we can easily calculate the time delay Δt for each geodesic, and $\Delta t = t_{\text{geo}} - t_{\text{obs}}$, where t_{geo} is the time used by a photon traveling from the observer to the disk following the geodesic. With Δt and the position of the spot, we can compute the distance between the intersection of the geodesic with the disk and the center of the spot, i.e., $|\mathbf{x} - \mathbf{x}_{\text{spot}}|$. Thus the emissivity can be computed readily.

In Figure 14, we illustrate the images of the spot with different black hole spins. As the spin increases, the marginally stable circular orbit is closer to the event horizon of the black hole, and the time delay effect becomes remarkable. The image of the spot is seriously warped, especially when the spot moves to the back of the event horizon.

When an image is obtained, the redshift and Gaussian emissivity of all points on the spot can be computed. Repeating this procedure over one period of the motion gives a time-dependent spectrum. Integrating the spectrum over frequency, or equivalently over the impact parameters, gives the light curve. The spectrum and light curve are shown in Figure 15, which agree well with the results shown in Figures 6 and 7 of Dexter & Agol (2009).

6.8. Radiative transfer

6.8.1. The radiative transfer formulation

In this section we give a brief discussion to the radiative transfer process under the Kerr spacetime. One can find more detailed discussions from Fuerst & Wu (2004) and Younsi et al. (2012). It is well known that $\mathcal{I} = I_\nu/\nu^3$, $\chi = \nu\alpha_\nu$ and $\eta = j_\nu/\nu^2$ are Lorentz invariants, where I_ν is the specific intensity of the radiation, α_ν and j_ν are the absorption and emission

coefficients at the frequency ν . The radiative transfer equation reads (Younsi et al. 2012)

$$\frac{d\mathcal{I}}{d\tau_\nu} = -\mathcal{I} + \frac{\eta}{\chi}, \quad (139)$$

where τ_ν is the optical depth at the frequency ν , and defined by $d\tau_\nu = \alpha_\nu ds$ and $ds = -p_\mu u^\mu d\sigma$, in which ds is the differential distance element of a photon traveling in the rest frame of the medium, σ is the affine parameter, p_μ is the four momentum of the photon, and u^μ is the four velocity of the medium. Then the radiative transfer equation can be rewritten as (Younsi et al. 2012)

$$\frac{d\mathcal{I}}{d\sigma} = -p_\mu u^\mu |_\sigma \left(-\alpha_\nu \mathcal{I} + \frac{j_\nu}{\nu^3} \right). \quad (140)$$

The solution of above equation is (Younsi et al. 2012)

$$\mathcal{I}(\sigma) = \mathcal{I}(\sigma_0) e^{-\tau_\nu(\sigma)} - \int_{\sigma_0}^{\sigma} \frac{j_\nu(\sigma'')}{\nu^3} \exp \left(- \int_{\sigma''}^{\sigma} \alpha_\nu(\sigma') |p_\mu u^\mu |_{\sigma'} d\sigma' \right) p_\mu u^\mu |_{\sigma''} d\sigma'', \quad (141)$$

where the optical depth is

$$\tau_\nu(\sigma) = - \int_{\sigma_0}^{\sigma} \alpha_\nu(\sigma') p_\mu u^\mu |_{\sigma'} d\sigma'. \quad (142)$$

As discussed in section 5.1, we can convert the independent variable from affine parameter σ to parameter p . Using $\sigma = \sigma(p)$ and $d\sigma = \Sigma dp$, we can rewrite the solution as the integration of parameter p (Yuan et al. 2009)

$$\mathcal{I}(p) = \mathcal{I}(p_0) e^{-\tau_\nu(p)} - \int_{p_0}^p \frac{j_\nu(p'')}{\nu^3} \exp \left(- \int_{p''}^p \alpha_\nu(p') |p_\mu u^\mu |_{p'} |\Sigma' dp' \right) p_\mu u^\mu |_{p''} \Sigma'' dp'', \quad (143)$$

where

$$\tau_\nu(p) = - \int_{p_0}^p \alpha_\nu(p') p_\mu u^\mu |_{p'} \Sigma' dp'. \quad (144)$$

With above formulae one can deal with radiative transfer problems without considering the scattering contributions to the absorption and emission coefficients as did by Yuan et al. (2009) and Younsi et al. (2012).

6.8.2. Radiative transfer in pressure supported torus

In section 6.3 we have discussed a rotationally supported torus and demonstrated its images. When the torus is optically thick, only the emissions come from the boundary surface are considered. When the torus is optically thin, all parts of the torus will do contributions

to the observed emissions. We need to consider the radiative transfer procedure along the ray inside the torus. To get the absorption and emission coefficients, we need to know the structure model of the torus, which determines the distributions of the temperature, mass density, pressure etc.

Firstly we construct the model of the torus, in which the torus is a perfect fluid and its energy-momentum tensor is given by (Younsi et al. 2012)

$$T^{\alpha\beta} = (\rho + P + \epsilon)u^\alpha u^\beta + P g^{\alpha\beta}, \quad (145)$$

where ρ is the mass density, P is the pressure, and ϵ is the internal energy, u^α is the four velocity of the fluid, and $g^{\alpha\beta}$ are the contravariant components of the Kerr metric. From the conservation law, namely $T^{\alpha\beta}{}_{;\beta} = 0$, we get the equation of motion of the fluid as follows (Abramowicz et al. 1978):

$$\frac{\partial_\alpha P}{\rho + P + \epsilon} = -u_{\alpha;\beta} u^\beta, \quad (146)$$

where the semicolon ; represents the covariant derivative, and $u_{\alpha;\beta} u^\beta = a_\alpha$ is the four acceleration of the fluid. For the torus is stationary and axisymmetric, we have $a_t = 0$, $a_\phi = 0$, and a_r, a_θ are given by (Younsi et al. 2012)

$$a_r = -\dot{t}^2 \left[M \left(\frac{\Sigma - 2r^2}{\Sigma^2} \right) (1 - a \sin \theta \Omega)^2 + r \sin^2 \theta \Omega^2 \right], \quad (147)$$

$$a_\theta = -\dot{t}^2 \sin 2\theta \left(\frac{Mr}{\Sigma^2} [a - (r^2 + a^2)\Omega]^2 + \frac{\Delta \Omega^2}{2} \right), \quad (148)$$

where $\dot{t} = u^t$ is the time component of the four-velocity, Ω is the angular velocity and takes the form of equation (127). They satisfy following equation

$$u^t = \frac{1}{\sqrt{-(g_{tt} + 2g_{t\phi}\Omega + g_{\phi\phi}\Omega^2)}}. \quad (149)$$

Since the torus is assumed to be radiation dominated, the pressure P can be regarded as the sum of gas pressure P_{gas} and radiation pressure P_{rad} , and

$$P_{\text{gas}} = \frac{\rho k_B T}{\mu m_H} = \beta P, \quad (150)$$

$$P_{\text{rad}} = \frac{\sigma T^4}{3} = (1 - \beta)P, \quad (151)$$

where k_B is the Boltzmann constant, μ is the mean molecular weight, m_H is the mass of a hydrogen, β is the ratio of gas pressure to the total pressure, and $\sigma = \pi^2 k^4 / 15 \hbar^3 c^3$ is the

black-body emission constant. From the above equations, one finally obtains

$$P = \hbar c \left[\frac{45(1 - \beta)}{\pi^2 (\mu m_{\text{H}} \beta)^4} \right]^{1/3} \rho^{4/3}, \quad (152)$$

$$kT = \hbar c \left[\frac{45(1 - \beta)}{\pi^2 \mu m_{\text{H}} \beta} \right]^{1/3} \rho^{1/3}. \quad (153)$$

Thus $P = \kappa \rho^\Gamma$, which implies that the state equation of the fluid is polytropic, therefore its internal energy is proportional to the pressure $\epsilon = P/(\Gamma - 1)$, and the equation of motion of the fluid (146) becomes

$$\left(\rho + \frac{\Gamma}{\Gamma - 1} P \right) a_\alpha = -\partial_\alpha P. \quad (154)$$

Substituting $\partial_\alpha P = \kappa \Gamma \rho^{\Gamma-1} \partial_\alpha \rho$ and $P = \kappa \rho^\Gamma$ into above equation, one obtains

$$\partial_\alpha \rho = -a_\alpha \left(\frac{\rho^{2-\Gamma}}{\kappa \Gamma} + \frac{\rho}{\Gamma - 1} \right). \quad (155)$$

Introducing a new variable ξ defined by $\xi = \ln(\Gamma - 1 + \kappa \Gamma \rho^{\Gamma-1})$, above equation is simplified as

$$\partial_\alpha \xi = -a_\alpha, \quad (156)$$

which implies that the vector $\mathbf{n} = (a_r, a_\theta)$ in the r - θ plane can be regarded as the normal vector of the contours of the density ρ . Thus if we use $\mathbf{t} = (dr, d\theta)$ to denote the tangent vector of the contours, we have $\mathbf{n} \cdot \mathbf{t} = 0$, or equivalently

$$a_r dr + a_\theta d\theta = 0. \quad (157)$$

If we use ds to denote the differential proper length of the tangent vector, we have

$$ds^2 = \mathbf{t} \cdot \mathbf{t} = g_{rr} dr^2 + g_{\theta\theta} d\theta^2, \quad (158)$$

where g_{rr} and $g_{\theta\theta}$ are the components of the Kerr metric, and $g_{rr} = \Sigma/\Delta$, $g_{\theta\theta} = \Sigma$. Solving the equations (157) and (158) simultaneously, we get a set of differential equations to describe the contours of density ρ

$$\frac{dr}{ds} = \sqrt{\frac{\Delta}{\Sigma}} \frac{|a_\theta|}{\sqrt{a_\theta^2 + \Delta a_r^2}}, \quad (159)$$

$$\frac{d\theta}{ds} = -\sqrt{\frac{\Delta}{\Sigma}} \frac{|a_r|}{\sqrt{a_\theta^2 + \Delta a_r^2}}. \quad (160)$$

If we introduce an auxiliary variable ζ defined by $d\zeta = \sqrt{\Delta/\Sigma}ds$, and substitute equations (147) and (148) into the above equations we get

$$\frac{dr}{d\zeta} = \frac{\psi_2}{\sqrt{\psi_2^2 + \Delta\psi_1^2}}, \quad (161)$$

$$\frac{d\theta}{d\zeta} = \frac{-\psi_1}{\sqrt{\psi_2^2 + \Delta\psi_1^2}}, \quad (162)$$

which have the exactly same forms with equations (123) and (124), where ψ_1 and ψ_2 are given by the equations (125) and (126). With these equations, the distributions of the mass density ρ of the torus now are readily to be computed by evaluating the integral of ξ from the torus center $r = r_k$, $\rho = \rho_c$ to the location (r, θ) along a path C which is orthogonal to the density contours everywhere. And the integral of ξ is

$$\xi = - \int_C a_r dr + a_\theta d\theta. \quad (163)$$

From the equations (152) and (153) one can get the total pressure and temperature distributions immediately with the given density ρ .

Knowing the structure model of the torus, the absorption and emission coefficients are now readily to be specified, with which we can discuss the radiative transfer process inside the torus. Using the above torus model, we shall give two examples of radiative transfer applications.

Firstly we consider a rather simple case, in which the torus is optically thin. The emissivity is taken to be proportional to the mass density ρ , i.e., $j_{em} \propto \rho$, and is independent on the frequency ν . The absorption coefficient α_ν is simply assumed to be zero. The torus parameters are $n = 0.21$, $r_k = 12 r_g$. The black hole spin a is 0.998. The ratio of gas pressure to total pressure β is 2.87×10^{-8} . In Figure 16 we draw the images of the torus, which is optically thin and radiation pressure dominated. We see that the emissions mainly come from the central region of the torus, where the density is higher. As the inclination angle of observer increases, the frequency shift of the emission caused by the Doppler boosting becomes larger. In this figure the false color represents the observed intensities of the emission, showing that the approaching side of the torus is brighter than the receding side especially at higher inclination angles.

Secondly, we mimic a more realistic case, namely the thermal free-free emission and absorption procedure, in which the torus is semi-opacity. The emission and absorption

coefficients of the torus for a photon at energy E_0 are given by (Younsi et al. 2012)

$$j(E_0) = \mathcal{K} \left(\frac{n_e}{\text{cm}^{-3}} \right)^2 \left(\frac{E_0}{\text{keV}} \right)^{-1} \left(\frac{\Theta}{\text{keV}} \right)^{-1/2} e^{-E_0/\Theta}, \quad (164)$$

$$\alpha(E_0) = B_1 \left(\frac{n_e}{\text{cm}^{-3}} \right)^2 \frac{\sigma_T}{E_0^2}, \quad (165)$$

where $\Theta = k_B T$, \mathcal{K} and B_1 are the normalization constants, n_e is the electron number density and $n_e = \rho/\mu m_H$, σ_T is the Thompson cross-section. The observed intensity images of the optically thick and semi-opacity torus are plotted in Figure 17. These images are quite different from those of an optically thin torus. The emissivity now depends on the temperature, which decreases towards to the outer surface of the torus, leading the limb darkening phenomenon. When the rays are nearly tangential to the layers of the torus, they will travel a longer distance and go through the outer, thus colder layers. While when the rays are perpendicular to the layers of the torus, they will travel a shorter distance and go through the inner therefore hotter layers. Consequently, the observed intensity at lower inclination angles will be much brighter than that at higher inclination angles (Younsi et al. 2012).

7. Discussions and conclusions

Following Dexter & Agol (2009) we have presented a new public code named ynogk for the fast calculating of null geodesics in a Kerr spacetime. The code is written by Fortran 95, and composed by a couple of modules. In which the object-oriented method has been used, which makes the addition of the code to one’s own readily.

In ynogk the B-L coordinates r and μ have been expressed as analytical functions of the parameter p . In these expressions, the Weierstrass’ and Jacobi’s elliptic function $\wp(z; g_2, g_3)$, $\text{sn}(z|k^2)$ and $\text{cn}(z|k^2)$ are used, since the reductions to Weierstrass’s standard integrals are much easier, in which only one real root of the equations $R(r) = 0$ and $\Theta_\mu = 0$ is required. The B-L coordinates t , ϕ and the affine parameter σ have been expressed as numerical functions of p . For a given p , the number of times of a photon reaches the turning points both in radial and poloidal motions is uniquely determined and needs not to be specified by the user.

Actually in addition to p , coordinates r , μ (or θ) can also be taken as the independent variables (Dexter & Agol 2009). The main reason of using p is that one can pay no attention to handle turning points, which has been done by the inner routines of our code. This virtue is convenient for a person who is not familiar with or has no interesting to the details of

the calculation of a geodesics in the Kerr spacetime. Another reason is that the value of p which corresponds to the termination of the geodesic—either at the infinity or the event horizon—is finite. Thus it is easier to handle p than r . In our code r and μ can also be taken as the independent variable. We provide a routine named **geokerr**, which can take r or μ as the independent variable. But the number of turning points should be prescribed.

With the expressions of all coordinates and affine parameter as functions of p , the ray-tracing problem, which determines the intersection of the ray with a target object, now becomes a root finding problem. The function $f(p)$ that describes the surface of the target object needs to be given by the user and the roots of equation $f(p) = 0$ correspond to the intersections. We provide a module named **pem-finding** to search the minimum root of this equation by the Bisection or the Newton-Raphson method. In addition, the observer-emitter problem can also be converted to a root finding problem, which requires one to solve a set of nonlinear equations. A module named **obs-emitter** based on the Newton-Raphson method to solve these equations is provided in our code. The routines in this module will return the solution, provided the coordinates of the emitter, r_{em} , θ_{em} and ϕ_{em} , are given.

We present a new set of formulae to compute the constants of motion λ and q from initial conditions. These formulae can be regarded as the extensions of Cunningham & Bardeen (1973). Our formulae are pervasive and can be used to handle more sophisticated cases, in which the motion state and the finite distance of the observer or the emitter with respect to the black hole are considered. One may find it is convenient when dealing with problems in which the emitter has motion and is closed to the vicinity of a black hole, e.g., the self-irradiation process in the inner region of a disk.

The code has been tested extensively with various toy problems in the literature. The results agree well with previous works. The comparisons with geokerr of Dexter & Agol (2009) also have been presented.

Finally we point out that the strategy discussed in this paper can be naturally extended to the calculation of the timelike geodesics almost without any modification. Especially for the timelike bounded orbits, in which the number of turning points both in poloidal and radial coordinates can be arbitrary. The extension of this strategy to calculate the timelike geodesics in a Kerr-Newmann spacetime has been done and the results are under preparation.

Acknowledgments

We acknowledge the financial supports from the National Basic Research Program of China (973 Program 2009CB824800), the National Natural Science Foundation of China

11163006, 11173054, and the Policy Research Program of Chinese Academy of Sciences (KJCX2-YW-T24). We also thank the anonymous referee for very creative and helpful comments and suggestions, which have improved both our work and the paper much.

REFERENCES

- Abramowitz, M., & Stegun, I. A. 1965, Handbook of mathematical functions with formulas, graphs, and mathematical tables (Dover Books on Advanced Mathematics, New York: Dover)
- Abramowicz, M., Jaroszynski, M., & Sikora, M. 1978, *A&A*, 63, 221
- Anderson, M., Lehner, L., Megevand, M., & Neilsen, D., 2010, *Phys.Rev.D*, 81, 04404
- Bardeen, J. M., & Petterson, J. A. 1975, *ApJ*, 195, L65
- Bardeen, J. M., Press, W. H., & Teukolsky, S. A. 1972, *ApJ*, 178, 347
- Beckwith, K., & Done, C. 2005, *MNRAS*, 359, 1217
- Broderick, A., & Blandford, R. 2004, *MNRAS*, 349, 994
- Broderick, A. E., & Loeb, A. 2006, *ApJ*, 636, L109
- Bromley, B. C., Chen, K., & Miller, W. A. 1997, *ApJ*, 475, 57
- Čadež, A., Fanton, C., & Calvani, M. 1998, *New Astronomy*, 3, 647
- Carlson, B. C. 1988, *Mathematics of Computation*, 51, 267
- . 1989, *Math. Comp.*, 53, 327
- . 1991, *Math. Comp.*, 56, 267
- . 1992, *Mathematics of Computation*, 59, 165
- . 2005, *J. Comput. Appl. Math.*, 174, 355
- Carter, B. 1968, *Physical Review*, 174, 1559
- Chandrasekhar, S. 1983, *The mathematical theory of black holes* (Oxford/New York, Clarendon Press/Oxford University Press)
- Cunningham, C. T. 1975, *ApJ*, 202, 788

- Cunningham, J. M., & Bardeen, C. T. 1973, *ApJ*, 183, 237
- Dexter, J., & Agol, E. 2009, *ApJ*, 696, 1616
- Dolence, J., Gammie, C. F., Mościbrodzka, M., & Leung, P. K., 2009, *ApJS*, 184, 387
- Fabian, A. C., Iwasawa, K., Reynolds, C. S., & Young, A. J. 2000, *PASP*, 49, 159
- Fanton, C., Calvani, M., de Felice, F., & Čadéz, A. 1997, *PASJ*, 49, 159
- Fuerst, S. V., & Wu, K. 2004, *A&A*, 424, 733
- Gebhardt, K., et al. 2000, *ApJ*, 539, L13
- Hopkins, P. F., Hernquist, L., Cox, T. J., & Kereš, D. 2008, *ApJS*, 175, 356
- Jaroszynski, M., & Kurpiewski, A. 1997, *A&A*, 326, 419
- Krolik, J. H. 1998, *Active Galactic Nuclei: From the Central Black Hole to the Galactic Environment* (Princeton: Princeton University Press)
- Laor, A. 1991, *ApJ*, 376, 90
- Li, L.-X., Zimmerman, E. R., Narayan, R., & McClintock, J. E. 2005, *ApJS*, 157, 335
- Luminet, J.-P. 1979, *A&A*, 75, 228
- Miniutti, G., & Fabian, A. C. 2004, *MNRAS*, 349, 1435
- Miniutti, G., & Fabian, A. C., & Miller, J. M. 2004, *MNRAS*, 351, 466
- Misner, C. W., Thorne, K. S., & Wheeler, J. A. 1973, *Gravitation* (San Francisco: W.H. Freeman and Co.)
- Müller, A., & Camenzind, M. 2004, *A&A*, 413, 861
- Noble, S. C., Leung, P. K., Gammie, C. F., & Book, L. G. 2007, *Class. and Quant. Gravity*, 24, 259
- Page, D. N., & Thorne, K. S. 1974, *ApJ*, 191, 499
- Press, W. H., Teukolsky, S. A., Vetterling, W. T., & Flannery, B. P. 2007, *Numerical recipes in FORTRAN. The art of scientific computing* (Cambridge: University Press, —c2007, 3rd ed.)
- Rauch, K. P., & Blandford, R. D. 1994, *ApJ*, 421, 46

- Reid, M. J., Broderick, A. E., Loeb, A., Honma, M., & Brunthaler, A. 2008, *ApJ*, 682, 1041
- Ruszkowski, M., & Fabian, A. C., 2000, *MNRAS*, 315, 223
- Schnittman, J. D. 2006, *ArXiv Astrophysics e-prints*, astro-ph/0601406
- Schnittman, J. D., & Bertschinger, E. 2004, *ApJ*, 606, 1098
- Schnittman, J. D., Krolik, J. H., & Hawley, J. F. 2006, *ApJ*, 651, 1031
- Schnittman, J. D., & Rezzolla, L. 2006, *ApJ*, 637, L113
- Schödel, R., & Ott, T., Genzel, R., Eckart, A., Mouawad, N., Alexander, T. 2003, *ApJ*, 596, 1015
- Shakura, N. I. 1987, *Sov. Astron. Lett.*, 13, 99
- Shakura, N. I., & Sunyaev, R. A. 1973, in *IAU Symposium, Vol. 55, X- and Gamma-Ray Astronomy*, ed. H. Bradt & R. Giacconi(Dordrecht: Kluwer), 155
- Shapiro, S. L., & Teukolsky, S. A. 1983, *Black holes, white dwarfs, and neutron stars: The physics of compact objects* (New York, Wiley-Interscience, 663 p.)
- Speith, R., Riffert, H., & Ruder, H. 1995, *Comp. Phys. Comm.*, 88, 109
- Sun, W. H. & Malkan, M. A. 1989, *ApJ*, 346, 983
- Viergutz, S. U. 1993, *A&A*, 272, 355
- Vincent, F. H., Paumard, T., Gourgoulhon, E., & Perrin, G., *ArXiv General Relativity and Quantum Cosmology e-prints*, gr-qc/1109.4769v1
- Wang, Y., & Li, X.-D. 2012, *ApJ*, 744, 186
- Wu, S.-M., & Wang, T.-G. 2007, *MNRAS*, 378, 841
- Younsi, Z., Fuerst, S.-V., & Wu, K. 2012, *A&A*, *ArXiv Astrophysics e-prints*, astro-ph/1207.4234
- Yuan, Y.-F., Cao, X., Huang, L., & Shen, Z.-Q. 2009, *ApJ*, 699, 722

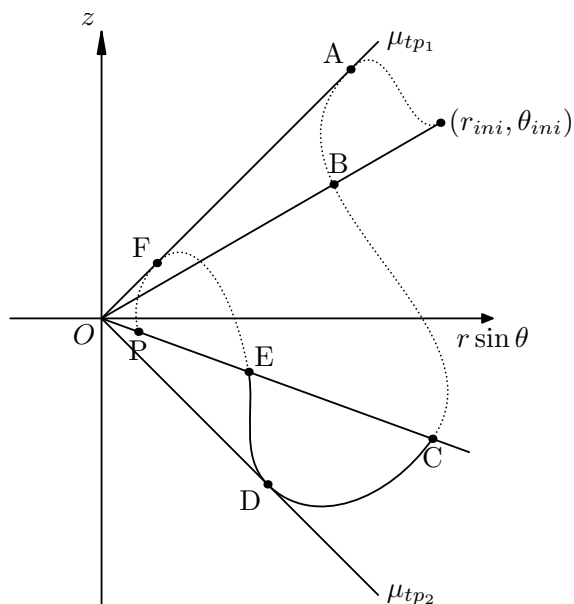


Fig. 1.— This figure illustrates the motion of a photon in the θ coordinate, which has been projected onto the $r - \theta$ plane. The motion is confined between two turning points μ_{p1} and μ_{p2} . A, D and F indicate the positions where the photon reaches the turning points and P indicates the position of the photon. The path between any two neighboring turning points (such as DA, DF) has the maximum monotonic length and the integrals of θ should be evaluated along each monotonic section and summed. The dotted (such as CA, EF and PF) and solid (such as DC and DE) lines represent the integral paths of I_1 and I_2 (see text) respectively. Obviously the BC section is the integral path of I_0 , and one has $I_0 = \int_B^C$, $I_1 = \int_C^A = \int_E^F = \int_P^F$, $I_2 = \int_D^C = \int_D^E$, etc.

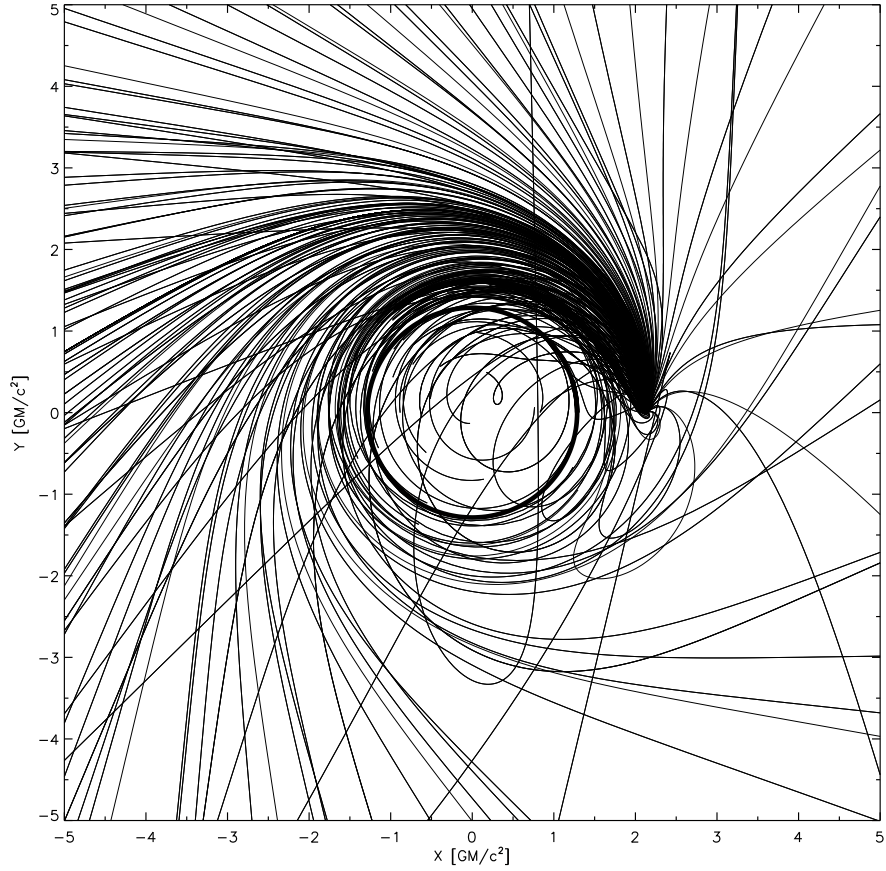


Fig. 2.— A set of geodesics emitted isotropically from a particle orbits around a black hole in the marginally stable circular orbit with $a=0.9375$. x and y are pseudo-Cartesian coordinates in the equatorial plane of the black hole. The figure shows the light bending and beaming effects clearly. A circle in the center represents the boundary of the event horizon.

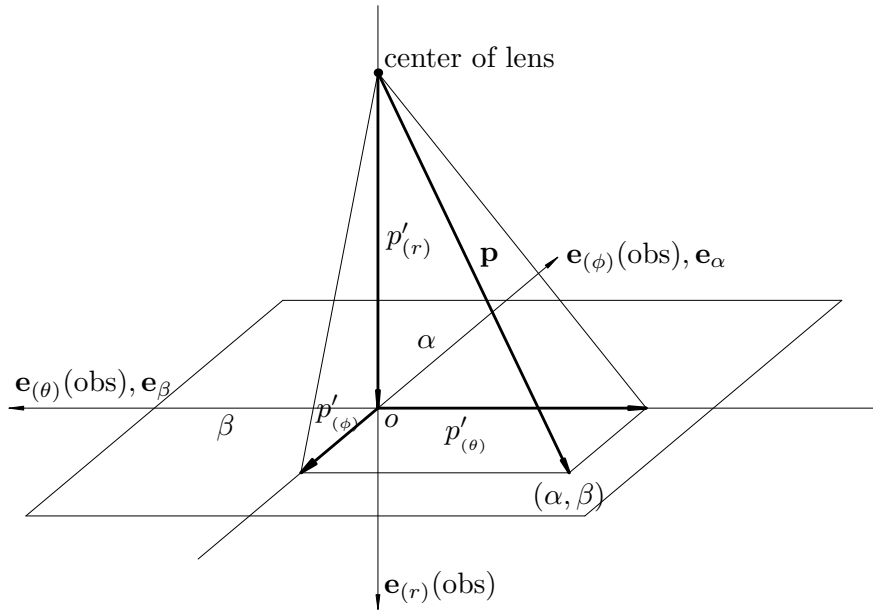


Fig. 3.— The figure shows the hitting of a photon on the photographic plate of the observer, from which the relationships between the impact parameters α, β and the components $p'_{(a)}$ of the four momentum of the photon are derived. Before hitting the plate, all photons will go through the center of the lens. $\mathbf{e}_{(r)}(\text{obs}), \mathbf{e}_{(\theta)}(\text{obs})$ and $\mathbf{e}_{(\phi)}(\text{obs})$ are the contravariant basis vectors of the frame, and the basis vectors of α, β coordinates $\mathbf{e}_\alpha, \mathbf{e}_\beta$ are aligned with $\mathbf{e}_{(\phi)}(\text{obs}), \mathbf{e}_{(\theta)}(\text{obs})$ respectively.

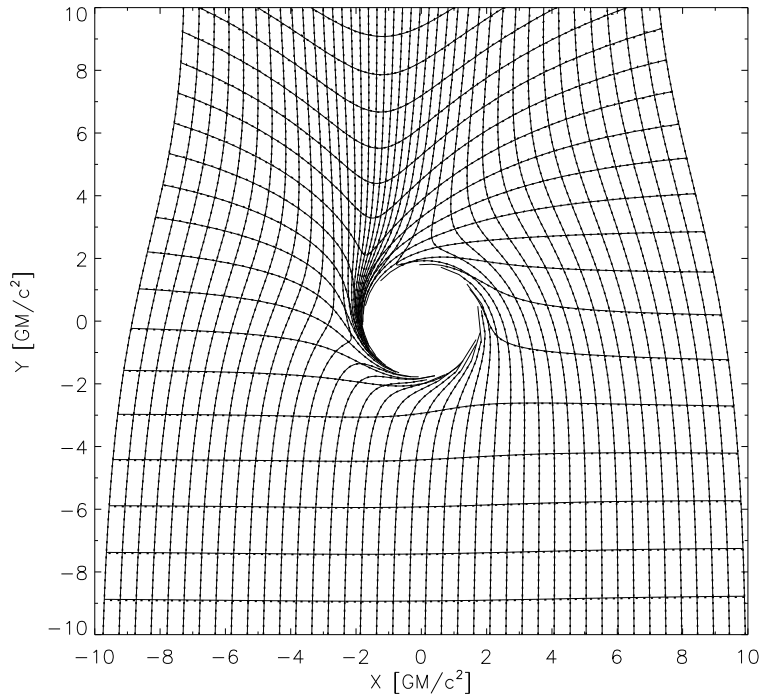


Fig. 4.— The projection of a uniform grid from the photographic plate of the observer onto the equatorial plane of a black hole is shown. The inclination angle θ_{obs} is 60° and the black hole spin a is 0.95. Solid lines represent the results from our code and the dotted lines from geokerr. x and y are pseudo-Cartesian coordinates in the equatorial plane of the black hole.

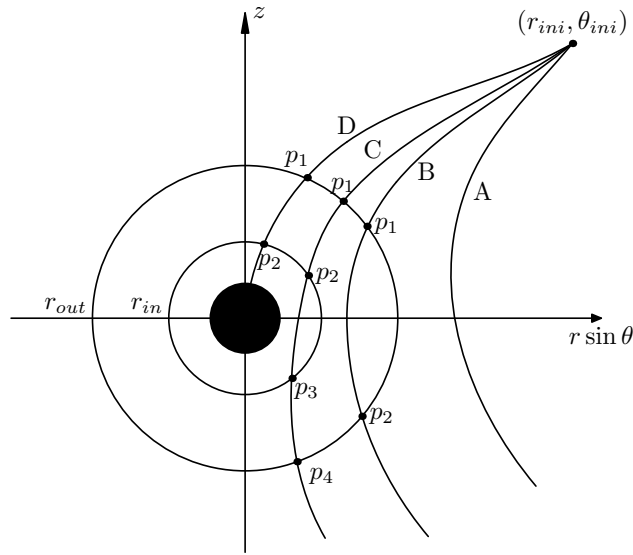


Fig. 5.— The classifications of a set of null geodesics according to their relationships with respect to a shell, the inner and outer radius of which are r_{in} and r_{out} respectively. The geodesics are classified into four classes, marked by A, B, C and D. Since the target object or the emission region are assumed to be completely included by the shell, only geodesics in classes B, C and D have probabilities to intersect with the target object or go through emission region. The trajectories of the geodesics are schematically plotted and have been projected onto the r - θ plane. The central black region represents the black hole shadow.

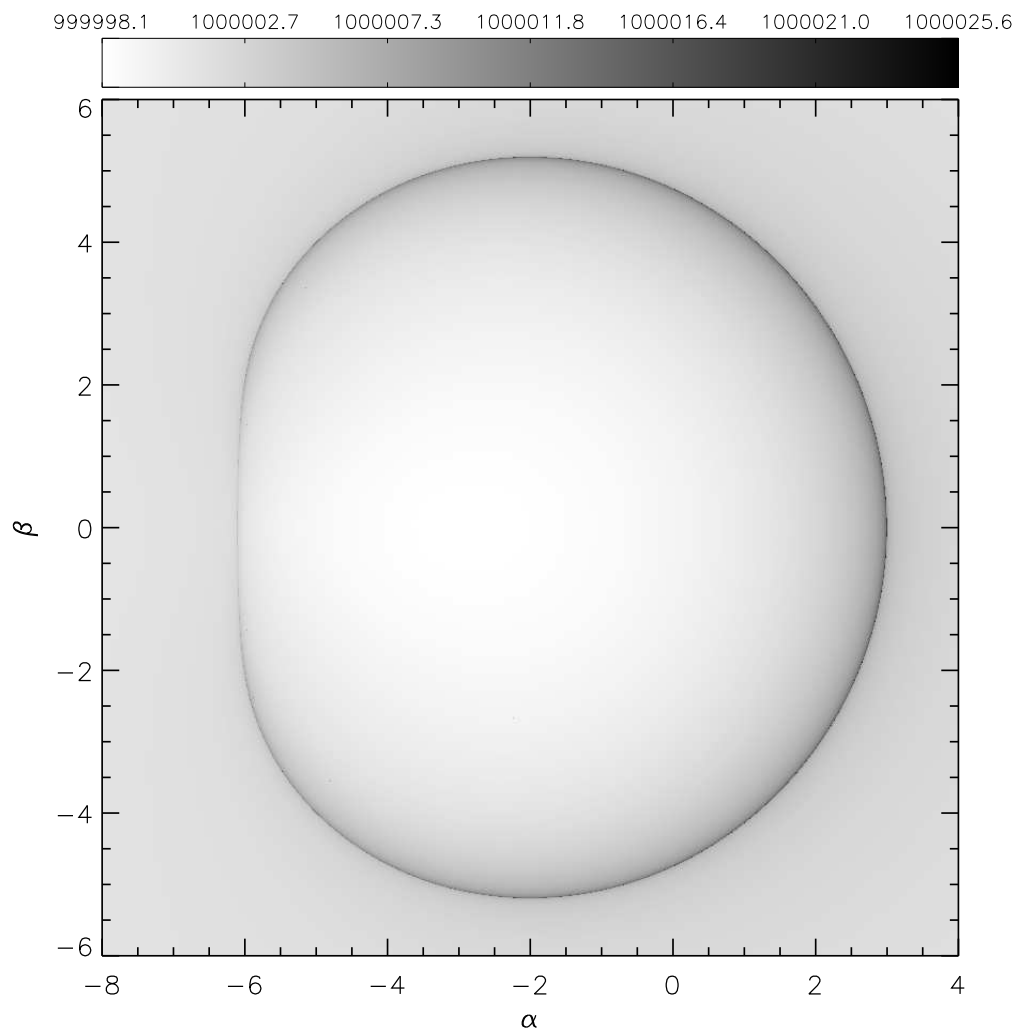


Fig. 6.— The shadow of a black hole with near extremal spin ($a = 0.998$) from the edge-on view is shown. The radial coordinate of the observer is $10^6 r_g$. The greyscale represents the value of the affine parameter σ evaluated from the observer to the terminated position—either at the black hole or re-emerging to the starting radius. Compare to Figure 2 of Dexter & Agol (2009). α and β are the impact parameters, which describe the size and the position of the image on the photographic plate.

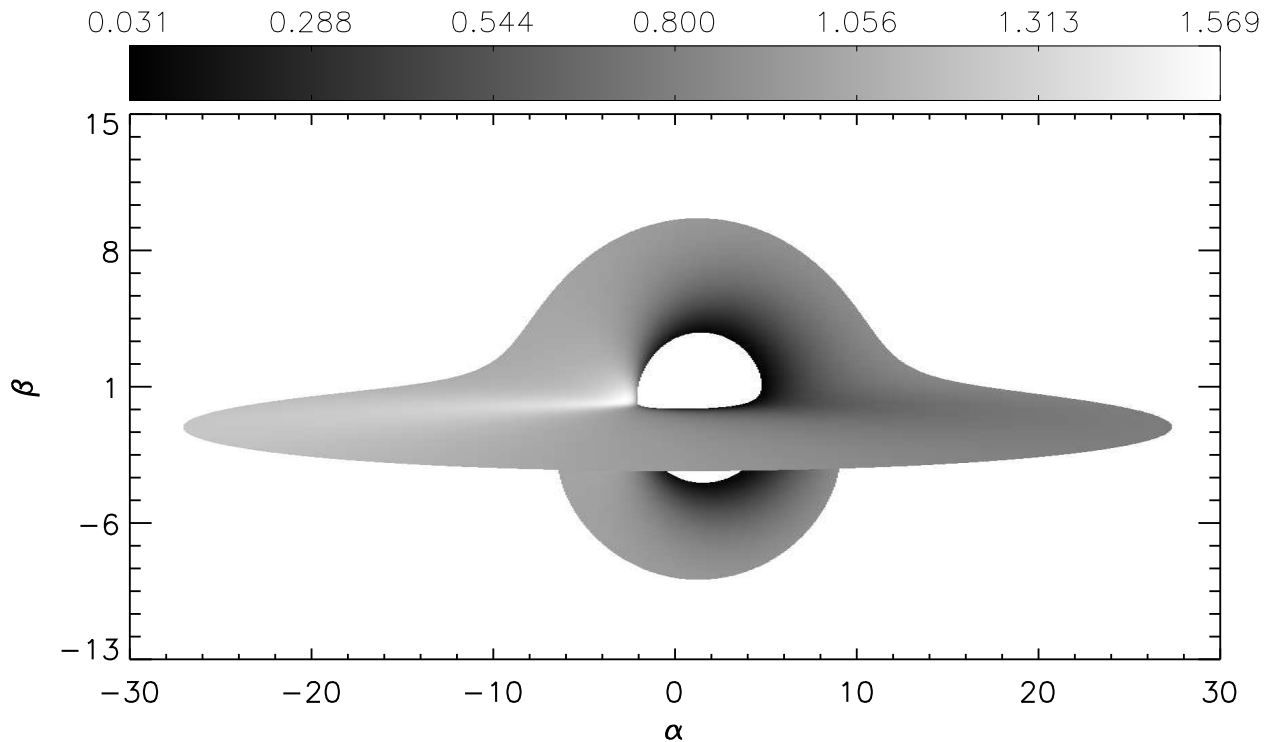


Fig. 7.— This figure shows the image of a standard thin accretion disk, whose inner and outer radius are r_{ms} and $22 r_g$ respectively. The black hole spin a is 0.998 and the inclination angle θ_{obs} is 86° . The radial coordinate of the observer is $40 r_g$. One can see Figure 6 of Beckwith & Done (2005) or Figure 4 of Dexter & Agol (2009) for comparison. The high-order image is also shown. α and β are the impact parameters, and the intensity of the greyscale represents the redshift g of emissions come from the surface of the disk.

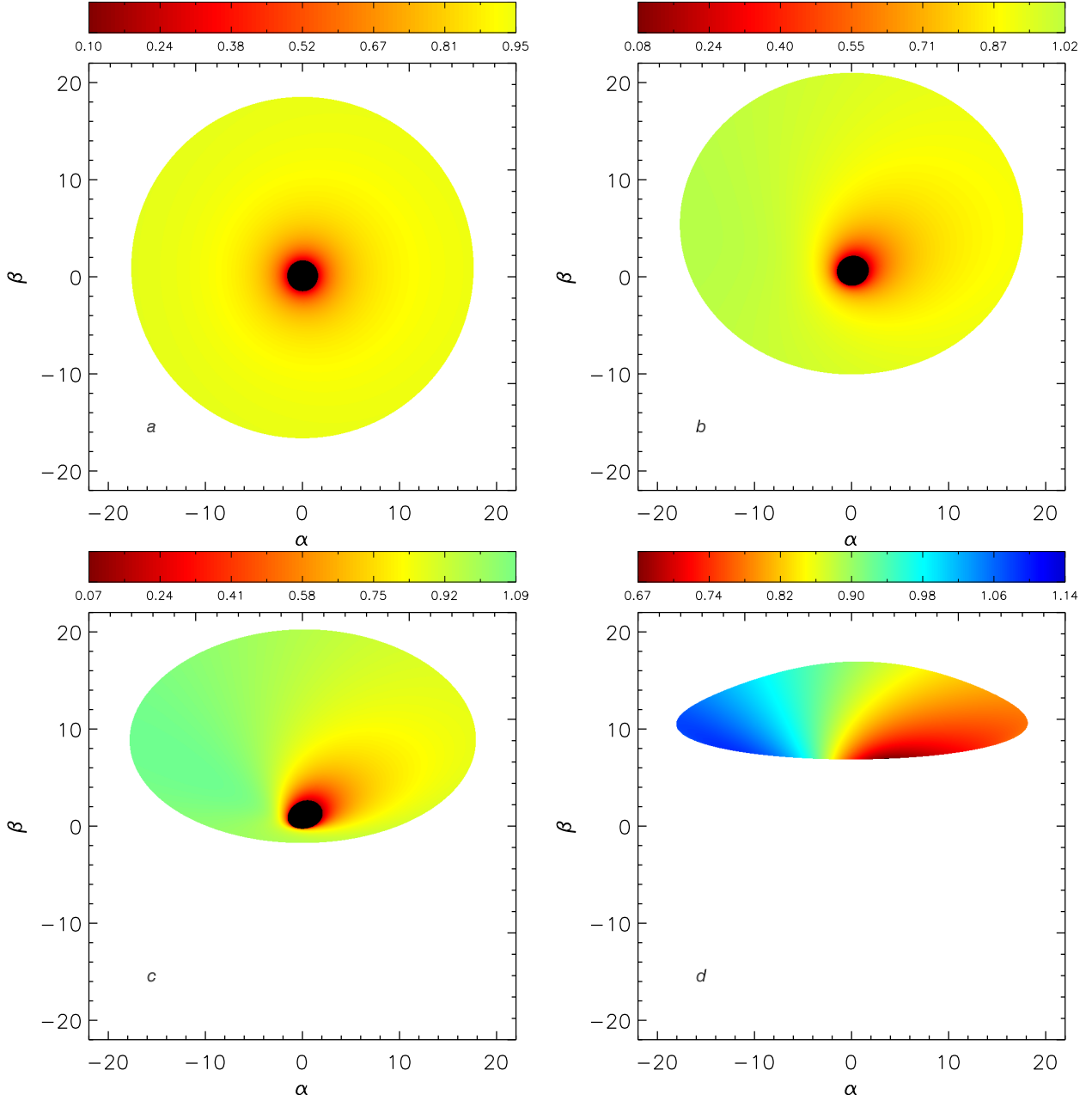


Fig. 8.— Images of a thick disk around a near extremal Kerr black hole ($a=0.998$) for various inclination angles are shown. The surface of the disk has a constant inclination angle δ with respect to the equatorial plane and δ is taken to be 30° . The inner radius is the marginally stable circular orbit r_{ms} and the outer radius is $20 r_g$. The inclination angles θ_{obs} are 5° , 30° , 55° and 80° for panels a, b, c and d respectively. α and β are the impact parameters, and the intensities of the color represent the redshift g of emissions come from the surface of the disk. Compare to Figure 10 of Wu & Wang (2007).

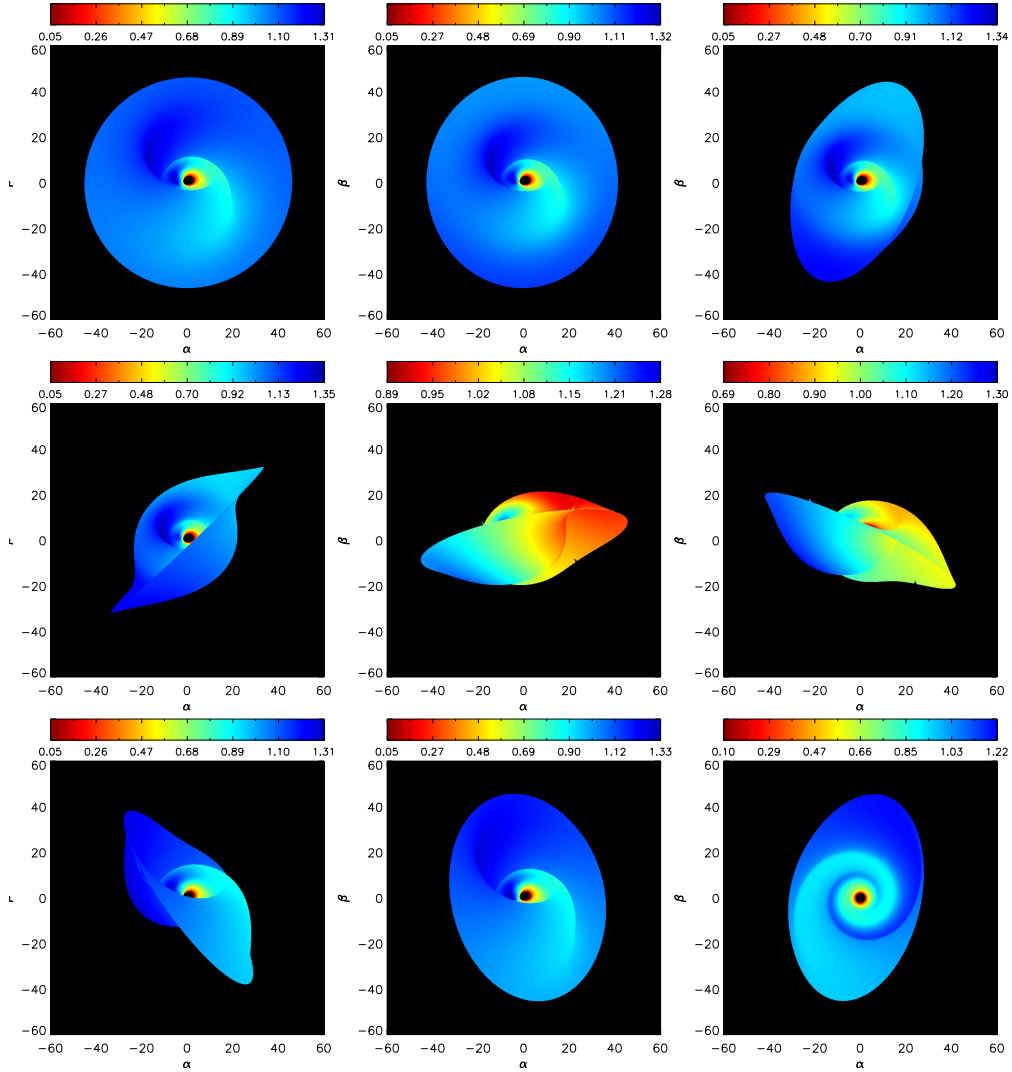


Fig. 9.— This figure shows the images of a warped accretion disk around a near extremal black hole ($a=0.998$) viewed from different azimuthal angles. The inner and outer radius of the disk are r_{ms} and $50 r_g$. The observer’s inclination angle θ_{obs} is 50° . The warping parameters are $n_1 = 4\pi$, $n_2 = 4$, and $n_3 = 0.95$. The azimuthal angle γ_0 , which represents the view angle, is 0° , 45° , 90° , 135° , 180° , 225° , 270° and 315° for panels from left to right and top to bottom respectively. For comparison we show a image observed from a face-on view in the final panel. The false color also represents the redshift g of the emissions come from the surface of the disk. α and β are the impact parameters. We take the parameter $n_1 \neq 0$, leading the warping of the disk along the azimuthal direction shown clearly in the final panel, which is the main difference compare to Figure 3 of Wang & Li (2012).

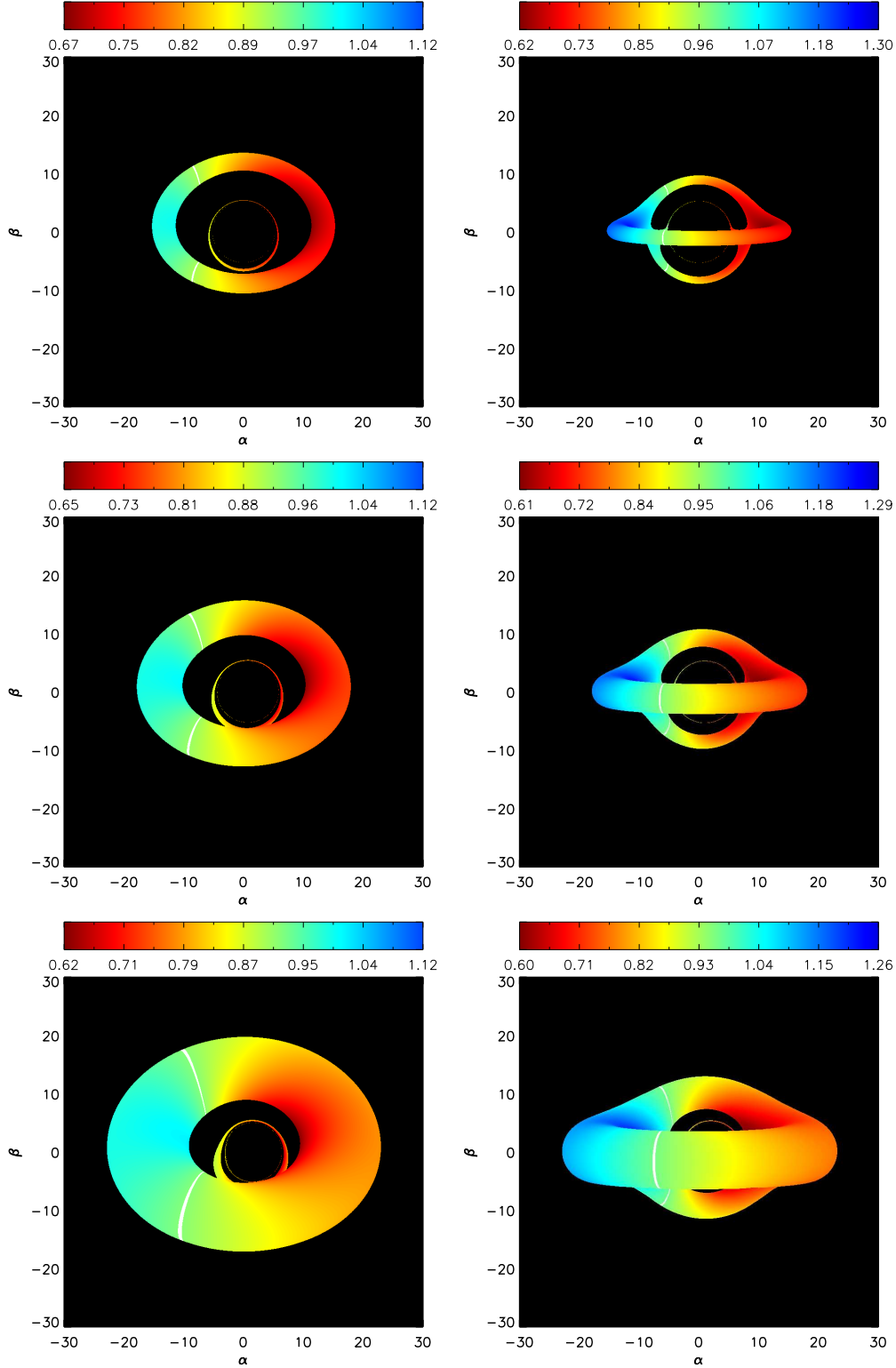


Fig. 10.— Images of a rotationally supported torus, which is geometrical and optically thick, are shown. The torus parameters are $n = 0.2$, $r_k = 12 r_g$. The black hole spin a is 0, 0.5 and 0.998 for panels from top to bottom. The inclination angle θ_{obs} is 45° for left column and 85° for right column. The false color represents the redshift g of the emissions come from the surface of the torus and the white areas represent the zero-shift regions. α and β are the impact parameters. Compare to Figure 3 of Younsi et al. (2012).

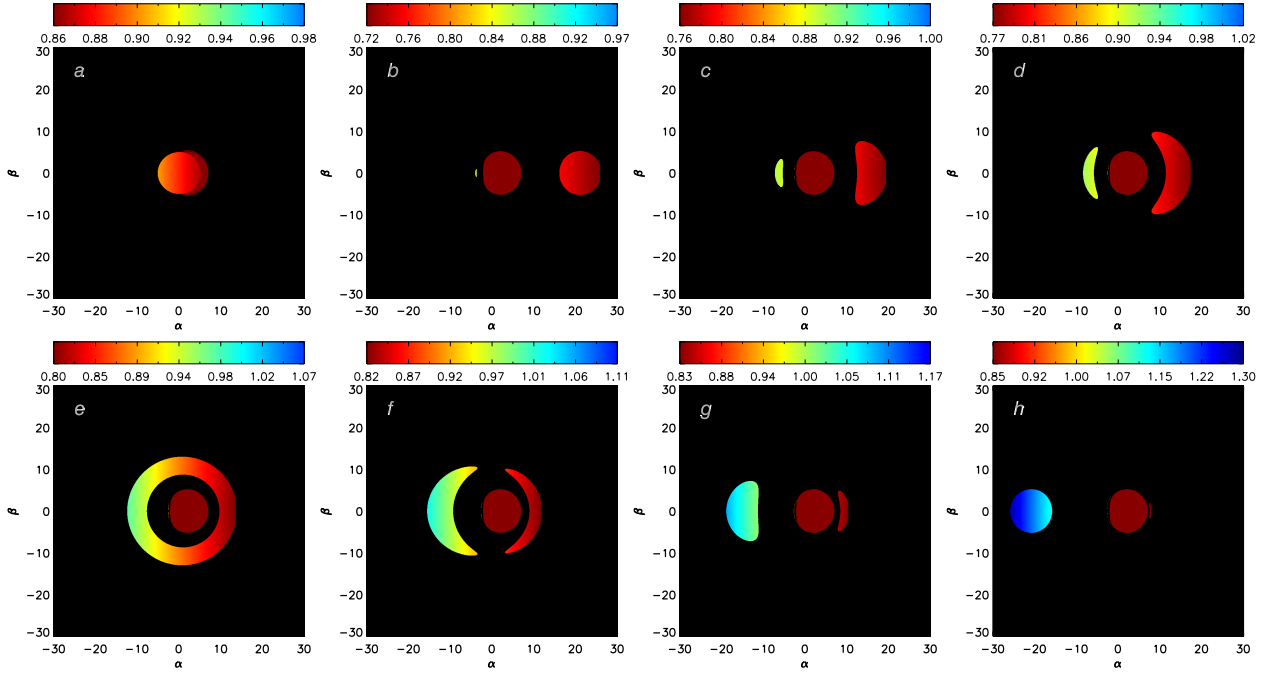


Fig. 11.— This figure illustrates the gravitational lensing effect by the motion of a ball movies around a near extremal black hole ($a=0.998$) in a Keplerian orbit. The motion is observed from an edge-on view. The radius of the ball and the orbit are $5 r_g$ and $20 r_g$ respectively. The central red region represents the black hole shadow. The azimuthal angles of the ball measured from the line of sight along inverse-clockwise direction are $0^\circ, 90^\circ, 150^\circ, 160^\circ, 180^\circ, 195^\circ, 210^\circ, 270^\circ$ for panels a-h. The pseudo color shows the redshift of the emissions come from the surface of the ball. α and β are the impact parameters.

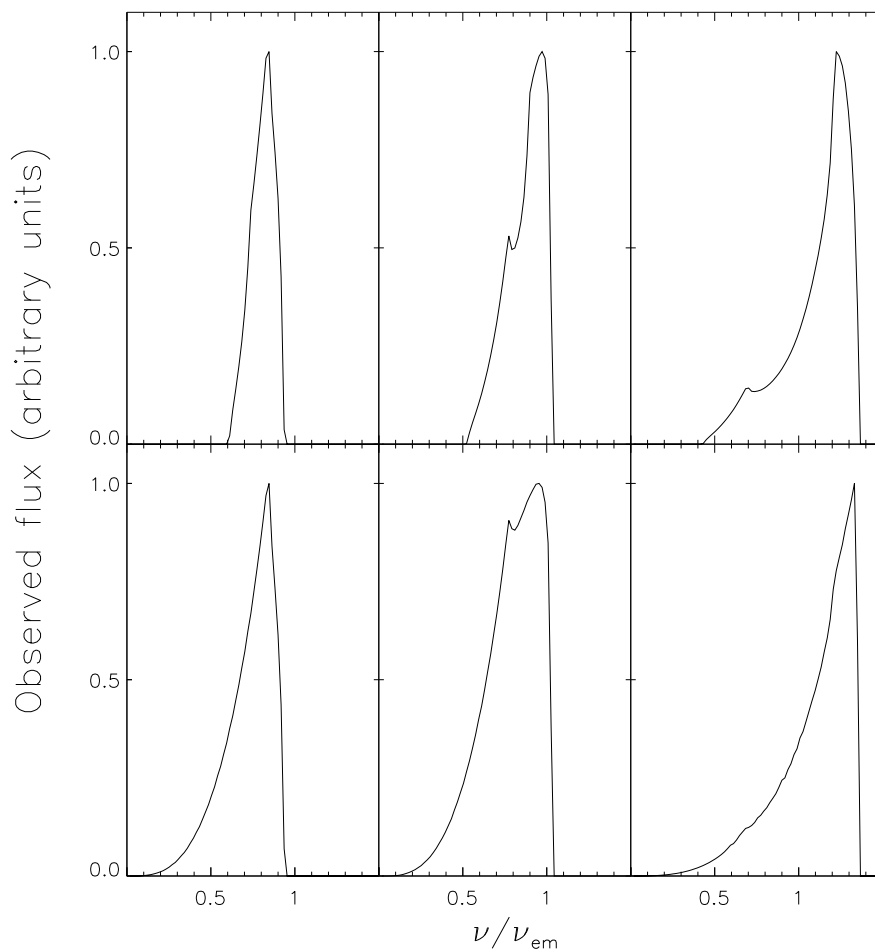


Fig. 12.— The theoretical line profiles of the Fe $K\alpha$ of a thin accretion disk for various black hole spins and inclination angles are shown. The inner and outer radius of the disk are r_{ms} and $15 r_g$. Top row: $a = 0.2$; bottom row; $a = 0.998$. Left column: $\theta_{obs} = 10^\circ$; middle column: $\theta_{obs} = 30^\circ$; right column: $\theta_{obs} = 75^\circ$. The horizontal and vertical axes represent the frequency and flux of the line respectively and are normalized. The line profiles are in agreement well with the Figure 3 of Čadež et al. (1998).

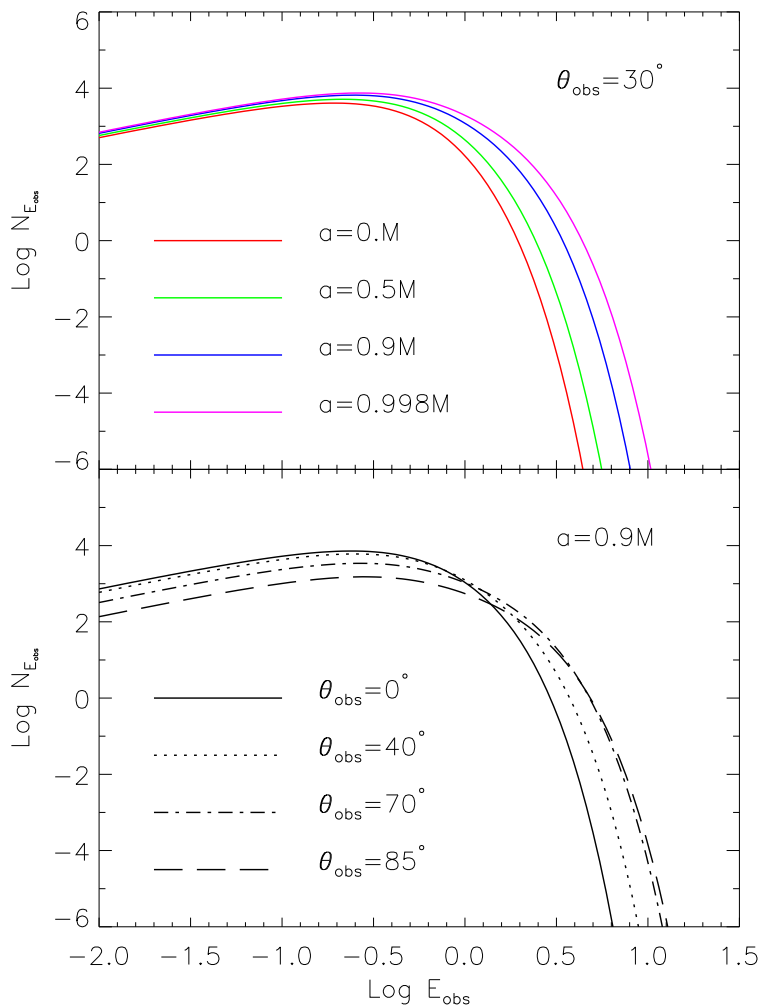


Fig. 13.— The effects of the black hole spin (top) and the inclination angle (bottom) on the spectrum of a standard thin accretion disk around a Kerr black hole are shown. The inner and outer radius of the disk are r_{ms} and $30 r_g$, where r_{ms} is the radius of marginally stable circular orbit.

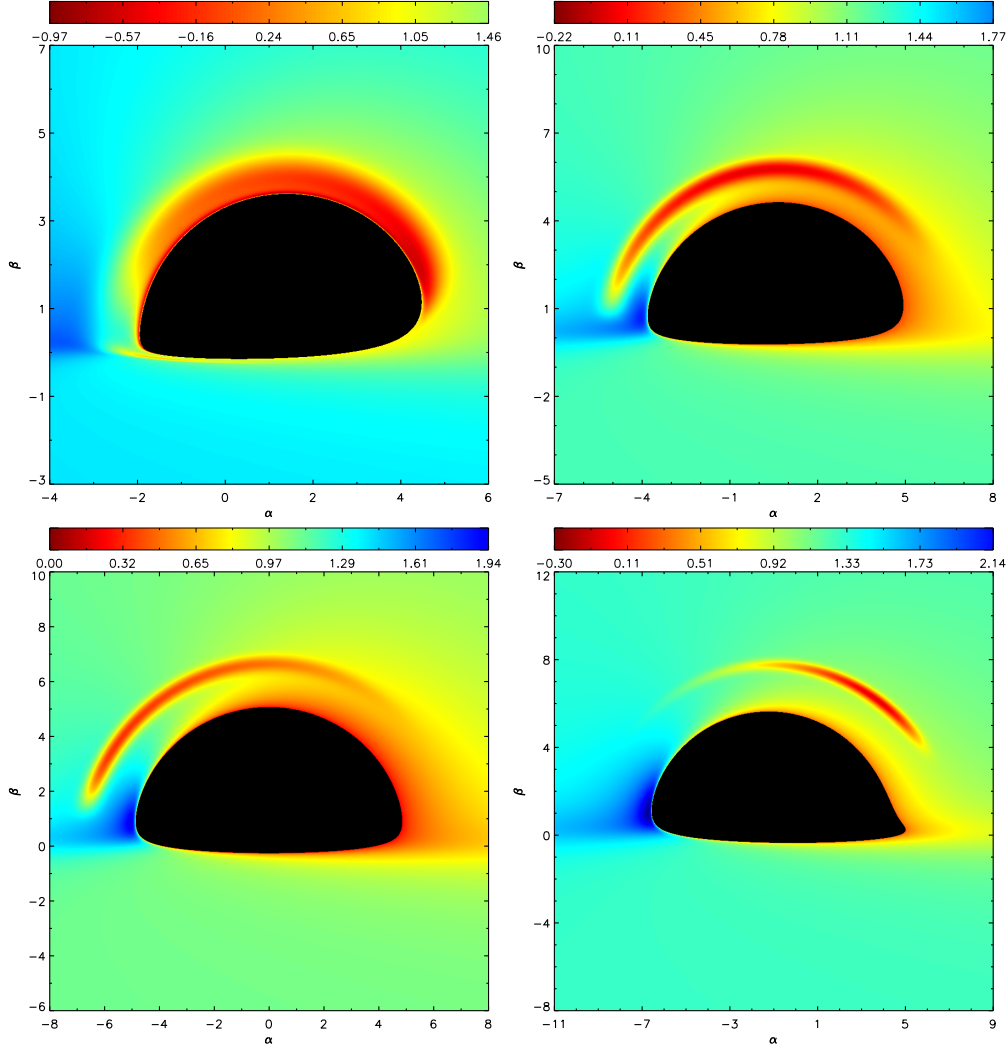


Fig. 14.— The images of a hot spot orbits around a black hole for different black hole spins are shown. The spot lies in a standard thin accretion disk and its central point is fixed at the ISCO. We have extended the inner radius of the disk to the photon orbit r_{ph} , at which the energy per unit rest mass of a particle is infinite. It is also the innermost boundary of circular orbit for particles (Bardeen et al. 1972). For the panels from left to right and top to bottom, the black hole spin a is 0.998, 0.5, 0 and -0.998 respectively. The inclination angle θ_{obs} is 85° . The false color represents the value of $g - j(\mathbf{x})$, where g is the redshift of the emissions come from the surface of the disk, and $j(\mathbf{x})$ is the emissivity of the spot.

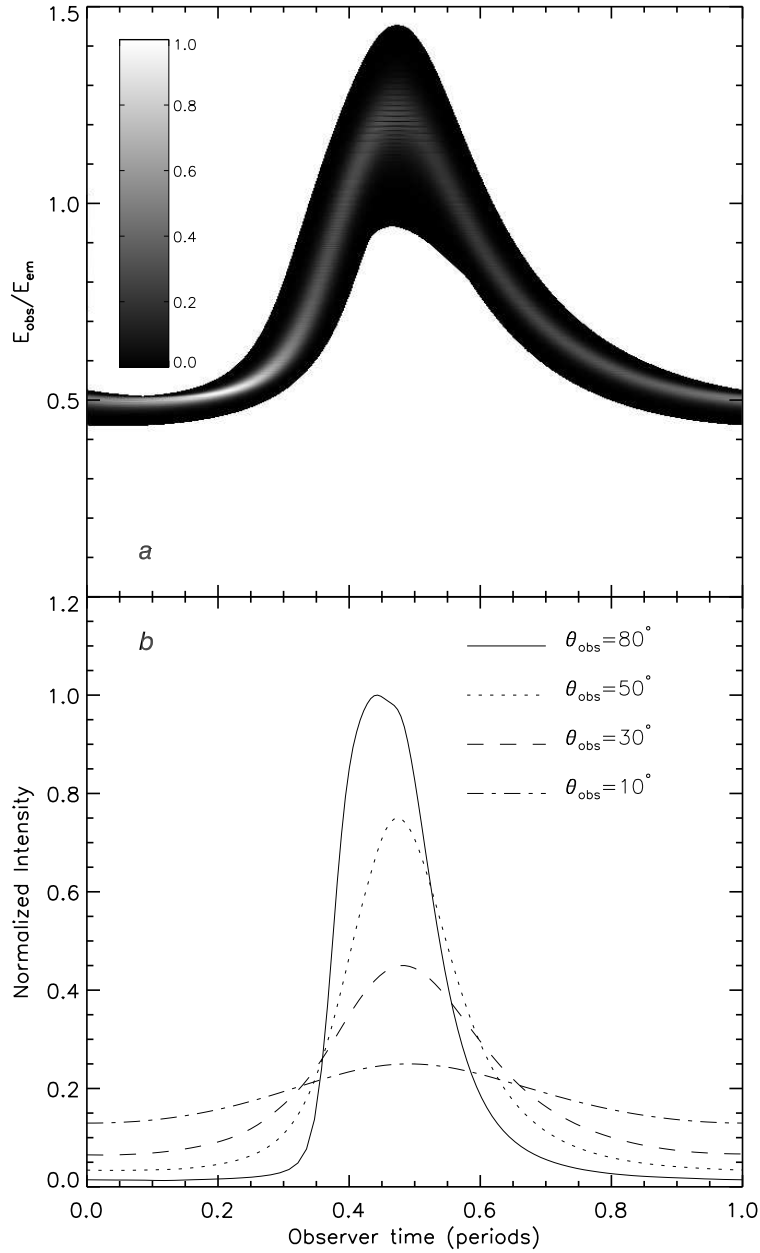


Fig. 15.— The time-dependent spectrogram (panel a) and light curves (panel b) of a hot spot orbits around a Schwarzschild black hole in the marginally stable circular orbit ($6 r_g$) over one period are shown. The inclination angle θ_{obs} is 60° for the spectrum. The greyscale in panel a represents total sum of emissivity $j(\mathbf{x})$ of emissions which are observed at the same time and have the same redshift g . The greyscale has been normalized and the maximum is taken to be 1. Compare to Figure 6 and 7 of Dexter & Agol (2009).

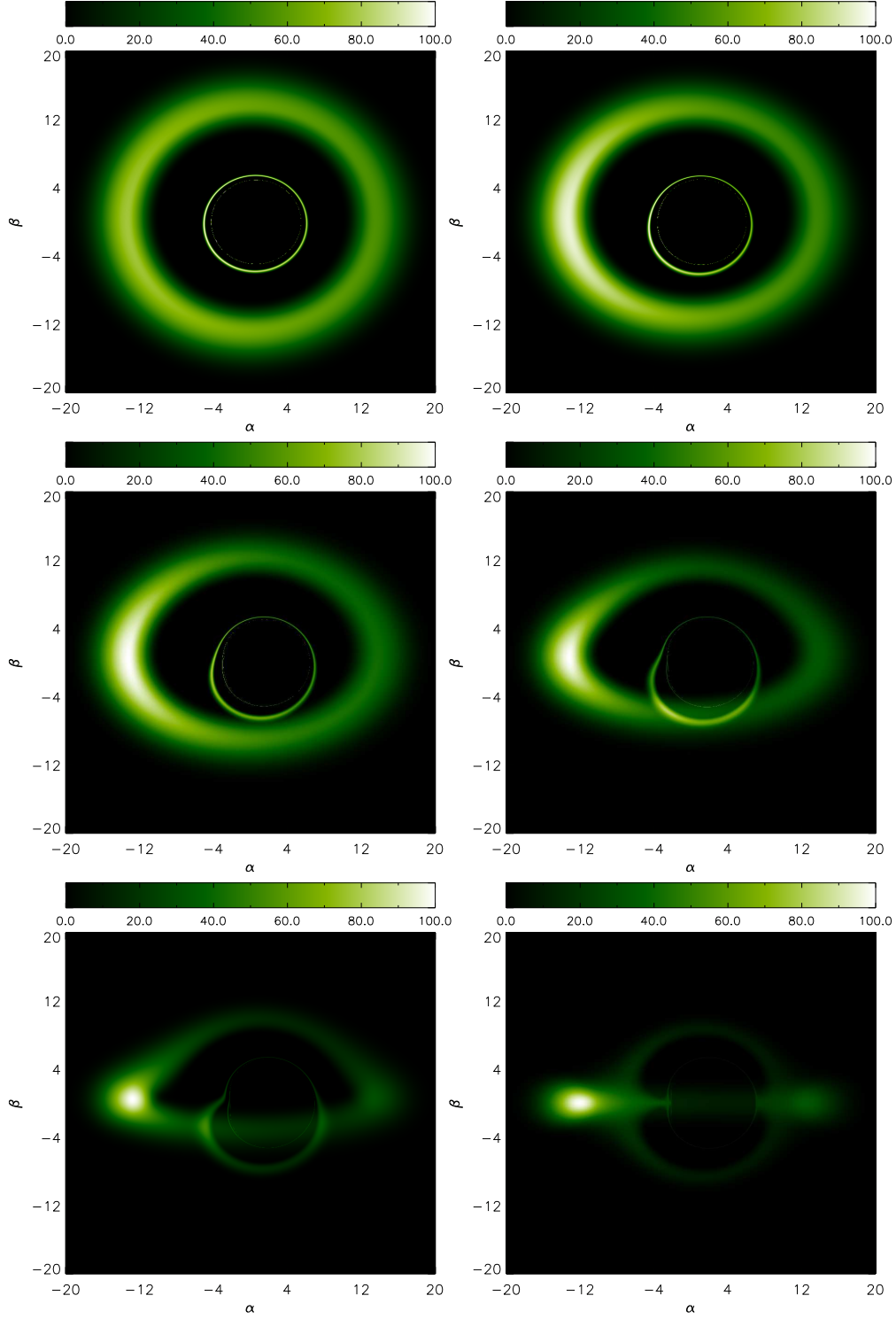


Fig. 16.— This figure shows the images of an optically thin and radiation pressure dominated torus. The inclination angles of the observer are 15° , 30° , 45° , 60° , 75° and 90° for panels from left to right and top to bottom. The black hole spin a is 0.998, and the ratio of gas pressure to total pressure β is 2.87×10^{-8} . The torus parameters are $n = 0.21$, $r_k = 12 r_g$. The brightness of each pixel represents the observed intensity integrated along a geodesic ray at a given frequency and has been normalized, and the maximum for each panel is the same and equals to 100. α and β are the impact parameters.

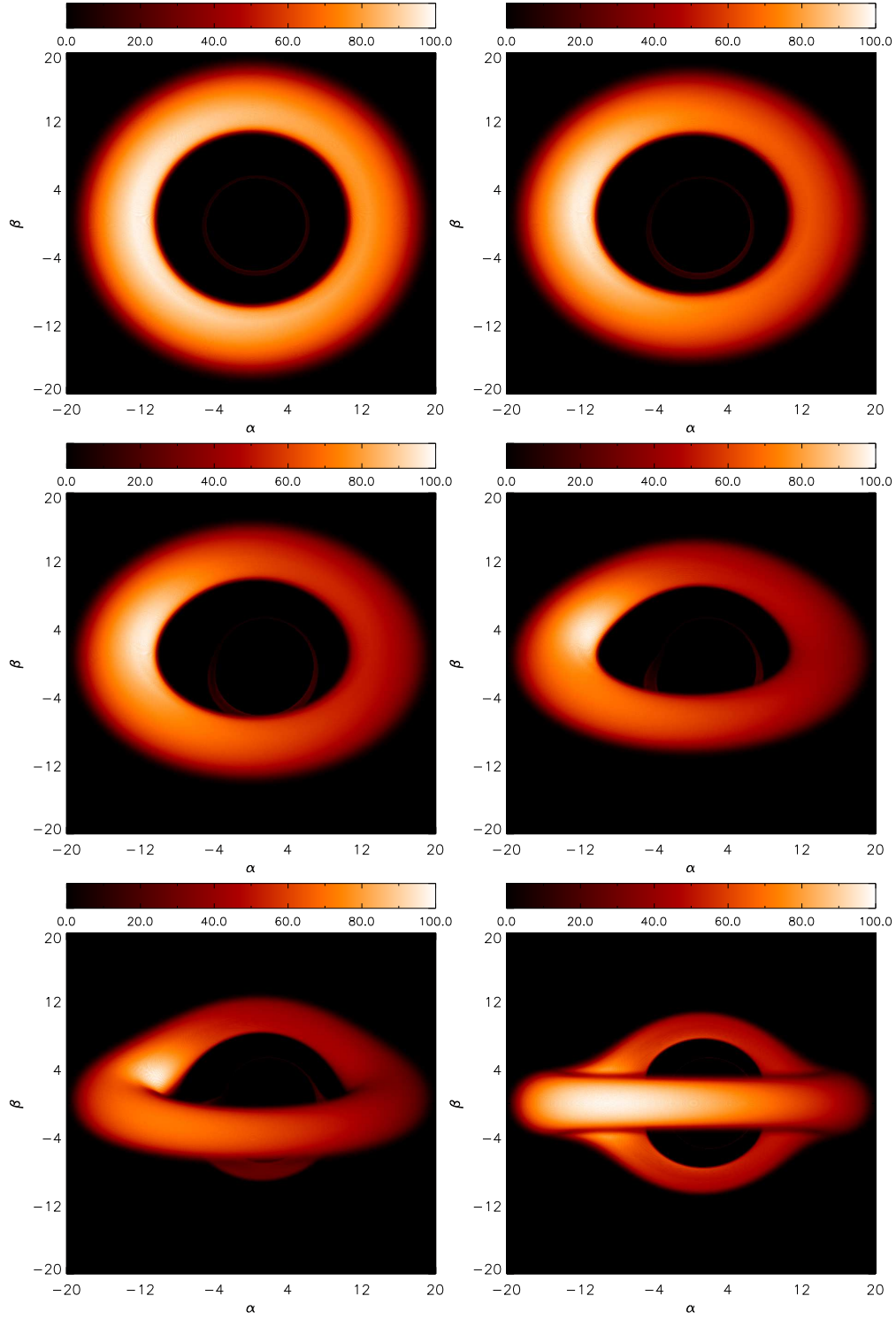


Fig. 17.— This figure shows the images of an optically thick and semi-opacity torus. The inclination angles are 15° , 30° , 45° , 60° , 75° and 90° for panels from left to right and top to bottom. The black hole spin a is 0.998, and the ratio of gas pressure to total pressure β is 2.87×10^{-8} . The torus parameters are $n = 0.21$, $r_k = 12 r_g$. The brightness of each pixel represents the observed intensity integrated over the entire spectrum. The intensity has been normalized, and the maximum of each panel is the same and equals to 100. α and β are the impact parameters.